

Chapter 4

Charge Transport in Organic Solar Cells

In this chapter, we simulate hole and electron transport within the framework of the multiscale model (Sec. 4.1 and 4.2). The kinetic Monte Carlo simulations are carried out on morphologies for pure, amorphous materials such as the donor polymer P3HT (Sec. 4.1.2) and the acceptor molecule PPDI (Sec. 4.2.2), as well as for two types of organic solar cells with bulk heterojunction, P3HT:DIPBI [72] (Sec. 4.1.3) and PBDT-TS1:PPDI (Sec. 4.2.6). (See Comp. Details 2.2)

4.1 Multiscale Model for Charge Transport in P3HT and P3HT:DIPBI

4.1.1 Introduction

Bulk heterojunction organic solar cells (BHJ-OSC) have been developed as a light-weight and low-cost alternative to conventional photovoltaic devices [9–16]. Commonly, they are composed of a donor polymer, e.g. poly(3-hexylthiophene) (P3HT) [70, 190, 273, 282, 299–305] and a fullerene-based acceptor, e.g. PCBM [306, 307]. However, due to the limited chemical tunability of fullerenes, a number of non-fullerene acceptors [47, 308], mostly perylene bisimide (PBI) derivatives [47, 309–319], have been proposed leading to rapidly increasing power conversion efficiencies of donor–acceptor blends [44, 63, 320, 321].

Although a number of rational considerations enter the development of this type of solar cell, it is still hard to predict its precise morphology, which plays a crucial role in the photovoltaic performance [8, 23, 32, 49, 322–330]. The morphology depends on a number of different factors such as the molecular weight of the donor and acceptor compounds [331–336], solvation effects [337], film processing [338, 339], regioregularity [301, 340], purity and mixing [341] of donor and acceptor materials [342] and post-treatment [343, 344]. Therefore, reliable theoretical predictions on the morphology of a particular blend depending on the fabrication protocol (e.g. annealing temperatures) and its influence on the device properties such as charge mobility would be extremely valuable. This presents a huge challenge to theoretical modelling, since it requires the combination of various methods designed for different time and length scales ranging from quantum mechanics on the molecular scale to kinetic Monte Carlo simulations on the morphological scale [57]. Such a multiscale simulation approach for photovoltaics has been proposed by Andrienko, Nelson and co-workers [53–58].

A similar approach [59] is adopted in this study, which aims to compute the charge carrier mobility in a blend of poly(3-hexylthiophene) (P3HT) and the non-fullerene acceptor tetrachlorinated diphenylene bisimide (DIPBI) [62, 63] (Fig. 4.1) via kinetic Monte Carlo simulations (kMC) [60, 61] using bimolecular charge-transfer rates based of Marcus theory [189], Jortner rates [207] and Weiss-Dorsey rates [201–204]. We use all three rate types for modelling intra- and intermolecular charge transfer.

The underlying morphologies were generated by coarse-grained (CG) molecular dynamics (MD) simulations at different annealing temperatures of 500 K, 700 K, and 900 K before cooling the system down to 300 K and backmapping the structure onto an atomistic representation [64]. Subsequently, the morphology is partitioned into charge residence sites (representing individual donor or acceptor molecules or fragments thereof) and charge hopping rates are computed using Marcus theory for all pairs of neighbouring sites. The hopping rates depend sensitively on the various quantities entering the Marcus formula, i.e. the internal and outer-sphere reorganization energies, site-energy difference, electronic coupling elements, and external driving forces. A number of different methods – both semiempirical and first principles – for calculating these quantities will be assessed with regard to their accuracy and computational speed. Finally, the computed hopping rates are employed in kMC simulations from which information on charge dynamics, including average site occupations and charge fluxes, is extracted and correlated to the morphology.

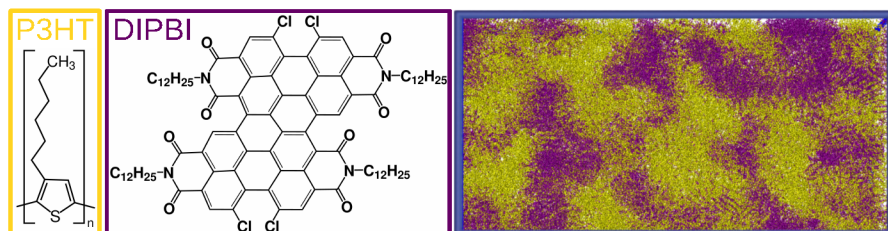


Figure 4.1: Structural formula of poly(3-hexylthiophene) (P3HT), where n is the number of thiophene units (left). Chemical structure of perylene bisimide dimer (DIPBI) (middle). Outtake of the P3HT:DIPBI blend morphology in atomistic representation (right).

It is generally assumed that the charge carrier mobility in P3HT is determined by the relative and absolute size of crystalline, semi-crystalline, and amorphous domains in the sample [345, 346]. In completely amorphous P3HT, the mobility has been determined to be of the order of $10^{-7} - 10^{-4}$ cm²/Vs by time-of-flight (TOF) measurements [299, 300] and carrier extraction by linearly increasing voltage (CELIV) [347, 348] and 10^{-5} cm²/Vs in field-effect transistors (FET) [273, 349]. The mobility depends crucially on the magnitude of the external electric field and temperature [248, 348]. The mobility in P3HT can rise significantly, when the fraction of crystalline regimes in the morphology increases [335], decreasing again at the onset of chain folding [350]. The upper bound is given by the mobility in pure crystalline P3HT in thin film with self-organized conjugated lamellae, which yield up to $\mu = 0.1$ cm²/Vs in FETs [190, 351–354].

Numerous correlations between the P3HT molecular morphology and the charge carrier mobility are discussed, such as an increasing fraction of crystalline regimes [355–357], an enhanced order in the $\pi - \pi$ -stacking direction [332], the order of the polymer backbone [327, 350, 358–360], and the interconnectivity of crystallite regions by tie chains [304, 327, 361]. Random orientation of crystalline domains and charge transport across domain boundaries reduce the mobility as compared to the perfect crystal [362, 363]. Hence, it is of major importance for efficient charge transport to bypass amorphous regimes [327, 364].

A desired tailoring of morphological features requires to understand and seize control of the molecular assembly processes and thus of the resulting solid-state short- and long-range order. Experimental studies report a peak in hole mobility as a function of molecular weight M_w , making it a potential tuning parameter due the direct impact on the evoked micro-structure [335, 336].

Going beyond the morphology and focusing on individual donor molecules within it, the mobility has been shown to strongly depend on the length and conformation of the polymer chains.

Theoretical transport models along a single polymer strand find an increase of mobility with chain length [365] and a saturation for sufficiently long chains [360]. This details that charge transport is strongly determined by the polymer conformation [327] and limited by chain folding [350]. In general, the appearance of rigid chains with few conformational defects leads to an increase in mobility [366]. The upper bound in mobility is found in pure crystalline P3HT in thin films with self-organised conjugated lamellae, which yield up to $\mu = 0.1 \text{ cm}^2/\text{Vs}$ in FETs [190, 351–354].

Charge carrier mobilities in P3HT:PCBM blends can be of the order $10^{-5}\text{--}10^{-4} \text{ cm}^2/\text{Vs}$ depending on the quota of regioregular P3HT in the blend [303, 367–369] and on the annealing temperature [303, 370]. The mobility can drop by four orders of magnitude in P3HT:PCBM in as-cast devices with respect to pristine P3HT, but can recuperate upon annealing [303]. The mobility in pristine PCBM films is higher by one order of magnitude than in the P3HT:PCBM blends [371, 372]. Increasing the PCBM content to 60–80 wt% increases electron mobility and accordingly improves performance for thicker devices [372].

DIPBI has been proposed [62, 63, 373] as a non-fullerene alternative to PCBM. The DIPBI molecule is made up of two linked perylene diimide (PDI) units and possesses a slightly twisted, non-planar geometry (Fig. 4.1).

In pure DIPBI organic single-crystal transistors, high charge carrier mobilities in the range of $\mu = 1.0\text{--}4.7 \text{ cm}^2/\text{Vs}$ [373] have been determined, higher than those of PCBM-based OFETs [303, 371, 372, 374], making it a promising candidate for solar cells. Indeed, a respectable PCE of 3.62% was measured in P3HT:DIPBI OSCs [63]. There are indications that a further increase in the PCE may be prevented by DIPBI's propensity to form large aggregated π -stacks [64]. The present work aims to unravel the role of DIPBI and the morphology in charge transport in P3HT:DIPBI blends. Moreover, the simulations will provide a fundamental understanding of the relation between charge transport and morphology which may prove useful for the future development of BHJ-OSCs.

4.1.2 kMC Simulations of Pure P3HT

4.1.2.1 Hole Mobility

As a first test of our model, we simulate the hole mobility in the well-studied system of amorphous pure P3HT. Our particular focus is on how different approximations made in the evaluation of the quantities entering the Marcus charge transfer rate affect the simulated charge carrier mobility.

We start with the P3HT morphology obtained from molecular dynamics simulations (see Computational Details 2.2). Here, we introduce the order parameter S to characterise the predominant alignment of the P3HT chains in the morphology. Therefore, we define a local coordinate system for each thiophene ring along the P3HT chain (see visual definition in Fig. 4.2 ,left). The origin of the local coordinate system is located at the centre of mass of the thiophene ring.

The vector \mathbf{n}_x (Fig. 4.2, yellow arrow) points to the sulfur atom and \mathbf{n}'_y towards the COM in the adjacent thiophene ring. \mathbf{n}_z (blue arrow) is the orthonormal vector to the thiophene plane $\mathbf{n}_z = \mathbf{n}_x \otimes \mathbf{n}'_y$, which is spanned by \mathbf{n}'_y and \mathbf{n}_x . Finally, we choose $\mathbf{n}_y = \mathbf{n}_x \otimes \mathbf{n}_z$ (white arrow) to guarantee the orthonormality. The vectors \mathbf{n}_i with $i \in [x, y, z]$ are determined for all $n=32$ thiophene rings along the P3MT chain (Fig. 4.2, right). By averaging for all similar \mathbf{n}_i in the morphology, a predominant direction vector $\bar{\mathbf{n}}$ is obtained.

With a set of \mathbf{n}_i and the predominant direction vector $\bar{\mathbf{n}}$ at hand, the order parameter S is defined as follows

$$S = \frac{3}{2} \left\langle (\bar{\mathbf{n}} \times \mathbf{n}_i)^2 - \frac{1}{3} \right\rangle . \quad (283)$$

In case that the order parameter has the value $S = 0$, then the system is in an isotropic phase. S has the value $S = 1$ for the nematic phase and it has $S = -\frac{1}{2}$, if all \mathbf{n}_i are orthogonal to $\bar{\mathbf{n}}$.

If we evaluate the order parameters in the P3MT morphology, we obtain small values, e.g. $S_{n_x} = 7.10 \times 10^{-4}$, $S_{n_y} = -9.42 \times 10^{-3}$ and $S_{n_z} = 1.25 \times 10^{-3}$. The order parameters clearly indicate that the system is in an amorphous phase. This corroborates our finding from visual inspection, where we note the absence of both crystalline regimes and extended spaces of parallel aligned P3HT lamellae.

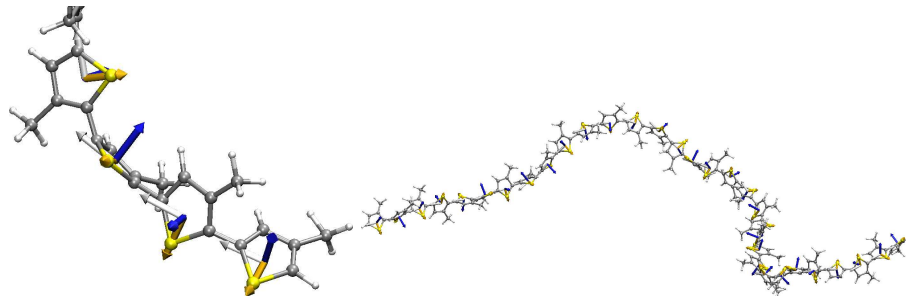


Figure 4.2: Visual representation of a local coordinate system in P3MT thiophene rings (left) and distribution along an entire P3MT $n=32$ polymer backbone (right). The origin of the local coordinate system is located at the centre of mass of the thiophene ring. \mathbf{n}_x (yellow arrow) points towards the sulfur atom, \mathbf{n}_y (white arrow) in the direction of the next thiophene ring and \mathbf{n}_z (blue arrow) is the normal vector of thiophene plane.

As a first approach to determine the charge carrier mobility, we treat each P3HT chain as a single molecule ($n = 32$) and compute the site energy contributions $E_i = E^{\text{el}} + E^{\text{pol}}$ for 416 P3HT (Fig. A.16), yielding an average energy of $\bar{E}_i = (-0.131 \pm 0.146)$ eV (Eq. 199). The average outer-sphere reorganization energy distribution is centred at $\bar{\lambda}_{\text{out}}^h = (0.157 \pm 0.014)$ eV (Eq. 228). In the unpartitioned P3HT 32mer morphology, we obtain $N_{\text{pairs}} = 20729$ charge transfer pairs at a cutoff radius of $r_{\text{NN}}^{\text{cut}} = 5$ nm, and $N_{\text{pairs}} = 21016$ in P3MT, if we substitute the side chains with methyl groups.

Regarding the intermolecular charge transfer integrals $|J_{AB}|$, the major drawback of treating each P3HT with $n=32$ segments as a single entity is that frontier orbitals are not necessarily localised in the region where two neighbouring molecules interact most strongly (see Sec. 3.1.2, Fig. 3.4). This often leads to tiny wavefunction overlaps and thus small values of $|J_{AB}|$, in turn yielding unphysically small charge transfer rates. As a consequence, a very low mobility of $\mu_{\text{tot}}^h = (1.73 \pm 4.04) \times 10^{-14}$ cm²/Vs was obtained from the kMC simulations with default ZINDO/MOO transfer integrals.

Neglecting of the side chains does not significantly alter the frontier orbital localisation and thus the charge transfer integrals, but the distribution of the site-energy differences $\Delta\overline{E}_{AB}^h = (2.3 \pm 106.6)$ meV (Eq. 199) in P3MT is more narrow than $\Delta\overline{E}_{AB}^h = (6.4 \pm 209.9)$ meV in P3HT (Fig. A.17). Furthermore, the distribution of the outer-sphere reorganization energies is centred at $\lambda_{out}^h = (0.181 \pm 0.092)$ eV in P3MT (Fig. A.18), and at $\lambda_{out}^h = (0.157 \pm 0.014)$ eV in P3HT. These aspects lead to an increased hole mobility of about one order of magnitude in P3MT 32mers of $\mu_{tot}^h = (2.65 \pm 19.2) \times 10^{-13}$ cm²/Vs compared to P3HT 32mers (using ZINDO/MOO transfer integrals).

In an improved approach, the P3HT polymer chains were partitioned into segments according to a cutoff dihedral angle of $\theta_{SCCS}^{cut} = 75^\circ$ (see Eq. 268 and Fig. 3.5). All quantities entering the Marcus rate were then calculated based on the individual segments except for the outer-sphere contributions. This opens up a large number of additional pathways leading to a dramatically higher mobility of $\mu_{tot}^h = (6.21 \pm 0.66) \times 10^{-9}$ cm²/Vs (using ZINDO/MOO transfer integrals), due to the ability of the charges to access different conjugated segments along the polymer chains.

As a further improvement, also the outer-sphere contributions, i.e. λ^{out} and ΔE^{out} , were calculated with respect to individual segments. In addition, intramolecular hole transport along different adjacent, conjugated segments in a P3HT polymer chain was now taken into account using the CDFT-based rates calculated in Section 3.1.7. Together with ZINDO/-MOO intermolecular charge transfer integrals, this leads to another increase in the total mobility by one order of magnitude to $\mu_{tot}^h = (9.01 \pm 47.0) \times 10^{-8}$ cm²/Vs.

In the following, instead of the ZINDO/MOO method for intermolecular charge transfer integrals $|J_{AB}|$, we use the (unscaled) DIPRO approach in combination with the different electronic structure methods ZINDO, DFTB/3OB, AM1 and PM3 in order to assess the impact on intermolecular hole transport (see the distributions in Sec. 3.1.3 for comparison).

The lowest charge carrier mobility of $\mu_{tot}^h = (1.34 \pm 7.76) \times 10^{-12}$ cm²/Vs is found for DIPRO/ZINDO. An increase by an order of magnitude to $\mu_{tot}^h = (5.41 \pm 11.9) \times 10^{-11}$ cm²/Vs is found for DFTB/3OB. The semiempirical methods AM1 and PM3 lead to very similar results of $\mu_{tot}^h = (1.84 \pm 0.25) \times 10^{-9}$ cm²/Vs and $\mu_{tot}^h = (1.85 \pm 0.14) \times 10^{-9}$ cm²/Vs, respectively. In a further step, we employ linearly scaled DIPRO/DFTB/3OB and DIPRO/PM3 charge transfer integrals to match our benchmark CDFT values (see Table 3.2). For DFTB/3OB, the linear scaling leads to an increase in the total mobility by more than one order of magnitude to $\mu_{tot}^h = (1.15 \pm 0.48) \times 10^{-9}$ cm²/Vs. Similarly, an increased mobility of $\mu_{tot}^h = (3.81 \pm 8.18) \times 10^{-8}$ cm²/Vs was obtained for PM3.

To study the effect of the outer-sphere contributions to the total mobility, we have also carried out kMC simulations in which the corresponding terms were switched off, i.e. by setting $\lambda^{out} = 0$ and $\Delta E^{out} = 0$. In combination with unscaled DIPRO/PM3 transfer integrals, we thus obtained a mobility of $\mu_{tot}^h = (1.87 \pm 4.00) \times 10^{-7}$ cm²/Vs. Comparison to the result obtained including outer-sphere contributions shows that they have a detrimental effect on hole mobility.

Experimental hole mobilities in completely amorphous, pure P3HT range from 10^{-7} to 10^{-4} cm²/Vs [299,300,303]. An even higher mobility of $\mu^{int} = 0.02$ cm²/Vs was measured for intrachain transport [375]. Typical time of flight experiments are performed with moderate external fields of the order of $F^{ext} = 1 \times 10^7$ V/m [273] to 1×10^8 V/m [299]. This range has also been used for theoretical modelling of photovoltaic materials [57], although the local field strength in the material is not strictly known due to possible screening effects [376], the emergence of space charges [377,378] due to (undesired) doping [379] and imbalanced charge transport [380,381].

However, the charge carrier mobility is known to be extremely sensitive to the applied external field [300]. This has also been found in recent theoretical studies using a lower external field of $F^{\text{ext}} = 1 \times 10^4$ V/m [282], resulting in a charge carrier mobility of $\mu \approx 10^{-4}$ cm²/Vs for amorphous P3HT.

To further investigate the influence of the external field strength, we have carried out kMC simulations at various values of F^{ext} between 1 and 10^{10} V/m. As one can see from Figure 4.3, the mobility monotonously increases with decreasing field strength. For $F^{\text{ext}} = 1 \times 10^4$ V/m, we obtain a mobility of $\mu \approx 10^{-4}$ cm²/Vs, in agreement with Adamo et al. [282]. Clearly, it is possible to obtain any mobility value by adjusting the external field including the experimental results. Therefore precise knowledge of the local electric field present in the material would be highly desirable.

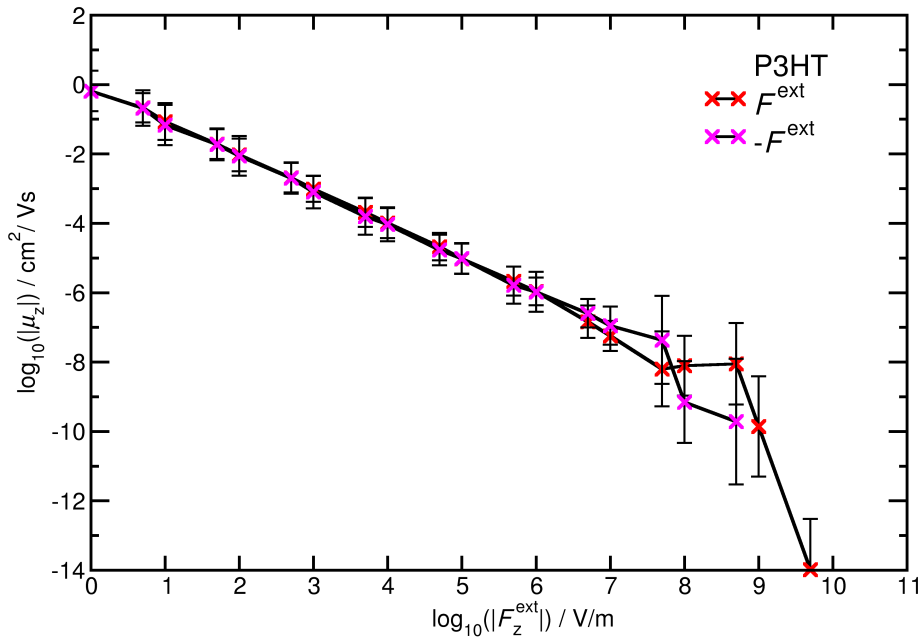


Figure 4.3: Field effect mobility μ_z for hole transport in P3HT morphology as a function of the external field F_z^{ext} from kinetic Monte Carlo simulations. If the external field is pointing in positive z direction, then the decadic logarithm of the external field has a positive sign and in the inverse case we employ a negative sign. Each kMC simulation has $N_{\text{steps}} = 1.0 \times 10^{10}$ steps, number of trajectories $N_{\text{kmc}} = 70$ per field strength.

The kMC simulations included CDFT-based intramolecular and DIPRO/PM3-based intermolecular hole transport, λ^{in} (B3LYP/6-311G*), $\lambda^{\text{out}} = 0.0$ eV, $\Delta E^{\text{out}} = 0.0$ eV.

Furthermore, there are a number of other approximations made in the multiscale modelling approach applied here that can potentially impact the mobility, e.g. finite size effects [248,382] or the reduction of the P3HT chain length to 32 segments, which corresponds to a molecular weight of 5.3 kDa. Experimentally, molecular weights ranging from 5 kDa to 72 kDa and beyond have been used resulting in mobility variations of up to two orders of magnitude [335,336,350,354,383]. Moreover, hole mobility crucially depends on the degree of crystallinity [356,357,360] and the locally ordered packing of chain segments [350,384] in the device [385], which in turn depends on the length of the polymers used. Such ordered domains are completely absent in our morphology, which is consistent with the low mobilities observed in our simulations.

To summarize, the choice of electronic structure method for the evaluation of the charge transfer integrals and the outer-sphere contributions influences significantly the simulated hole mobility. From the comparison of our kMC results with literature values, we conclude that charge transfer rates based on Marcus theory using the scaled DIPRO/PM3 method for interchain charge transfer integrals and the CDFT-based intrachain charge transfer integrals in combination with outer-sphere reorganization energies as well as electrostatic and polarisation contributions to the site-energy difference constitute a good compromise between accuracy and computational effort for the determination of the hole mobility in amorphous P3HT.

4.1.2.2 Site Occupation and Current

Visual inspection of the hopping site occupation numbers inside the P3HT morphology shows that there are densely packed regions with elevated average occupation numbers connected by isolated filamentary polymer chains with even higher occupation numbers (Fig. A.14). The average occupation numbers \bar{p} of the hopping sites in P3HT decrease from $n = 1$ to $n = 4$ and tend to increase with the conjugated segment length for $n > 4$ (Fig. 4.4,i). A similar observation can be made for the local current albeit with more pronounced local deviations from the overall trend (Fig. 4.4,ii).

Around 7.5% of all sites are never occupied in the kMC simulations. These unoccupied sites are mainly short segments with a length of $n = 1$ to $n = 8$. Of these, 20% are single thiophene rings, segments with lengths of $n = 2$ to $n = 6$ account for a roughly equal share of about 13%, and about 5% have $n = 7$ and $n = 8$. They are randomly scattered in the simulation box so that no contiguous unvisited regions can be identified.

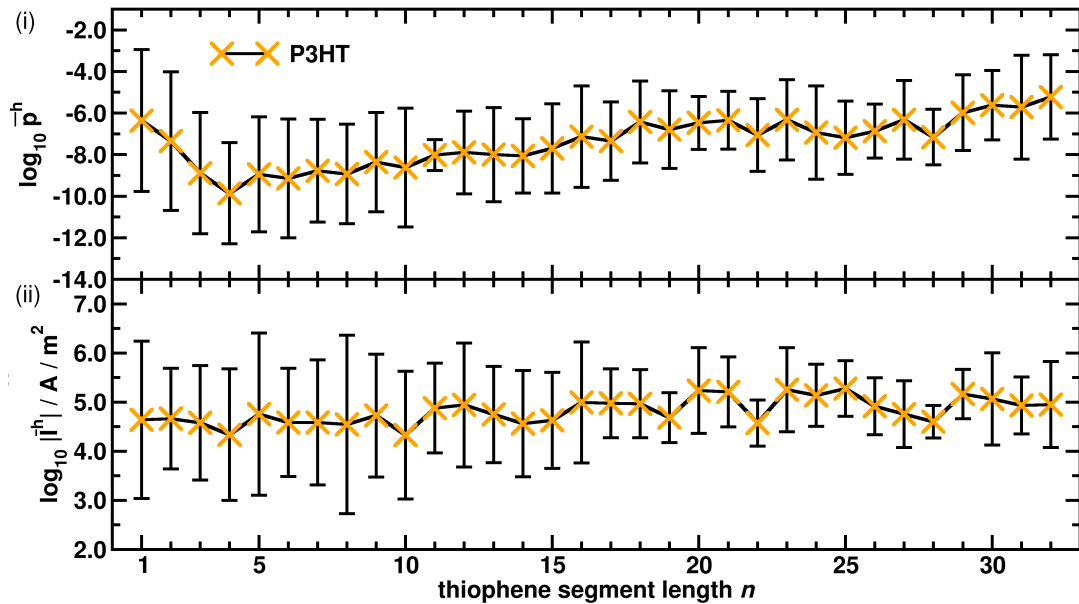


Figure 4.4: (i) Decadic logarithm of average hole occupation numbers $\log_{10} \bar{p}^h$ of hopping sites as a function of the thiophene segment length n in the P3HT morphology from kMC simulations with holes at an external field $F_x^{\text{ext}} = 1.0 \times 10^7 \text{ V/m}$. (ii) Average current density per hopping site $|\bar{I}^h|$ for hole transport.

4.1.3 kMC Simulations in P3HT:DIPBI

4.1.3.1 Morphologies

In the following, we will focus on the characterization of the three different P3HT:DIPBI morphologies generated with annealing temperatures of 500 K, 700 K, and 900 K in coarse grained simulations. First we analyse the planarity of the P3HT chains and then describe the stacking behaviour of DIPBI in the blend.

We can define a planarity descriptor P^b (Eq. 279) for individual P3HT chains with segment length $n = 32$ and determine its distributions for all chains inside the morphology, and compare the average values \bar{P}^b for an entire blend morphology (Fig. 4.5).

The three morphologies obtained at 500 K, 700 K, and 900 K give very similar values of $\bar{P}^b = 7.66 \pm 0.96$, 7.63 ± 0.93 and 7.75 ± 1.00 , respectively. In contrast, the value for pure P3HT is much higher ($\bar{P}^b = 17.95 \pm 1.07$), meaning that the planarity of the P3HT chains decreases significantly in the presence of DIPBI. The width of the distributions remains basically constant. This is corroborated by our finding that conjugated segments are typically longer in pure P3HT (Fig. 2.2).

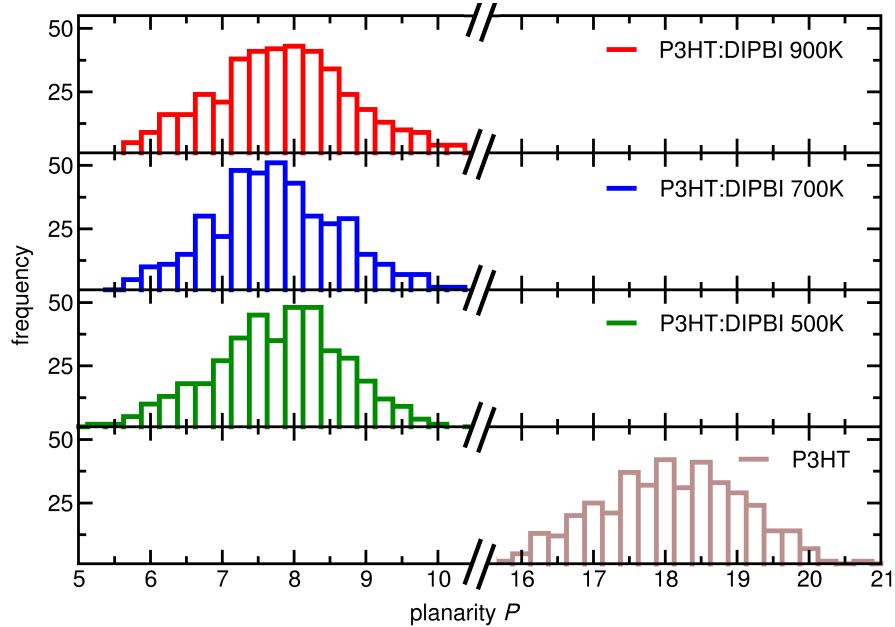


Figure 4.5: Distributions of the number of planarity descriptor P^b for the P3HT with thiophene chain length $n = 32$ inside the atomistic P3HT:DIPBI blend morphologies for three different CG annealing protocols [64] at 500 K, 700 K and 900 K and in amorphous P3HT for comparison.

In order to characterise the aggregation patterns of DIPBI, we calculated the intermolecular distance $d_{AB} = |\mathbf{d}_B - \mathbf{d}_A|$ and the angle $\alpha = \arccos(\mathbf{n}_A \cdot \mathbf{n}_B)$ enclosed by the two normal vectors \mathbf{n}_A and \mathbf{n}_B for every pair of DIPBI molecules A and B within a 15 Å radius (see Sec. A.1.7 for the precise definition of d_{AB} , $\mathbf{n}_{A,B}$ and visual illustration Fig. A.15). The density plots shown in Fig. 4.6 illustrate the frequency with which distinct relative DIPBI/DIPBI arrangements occur in the simulation box as a function of d_{AB} and α . The DIPBI molecules are seen to favour $\pi-\pi$ -stacking with the molecular planes aligned parallel to each other. This is indicated by the bright areas around $\alpha = 0^\circ$ and $\alpha = 180^\circ$.

In the density plot for the 500 K morphology, a bright spot is visible at about $d_{AB} = 4.0 \text{ \AA}$, which can be attributed to nearest neighbour stacking. The bright feature extends up to $d_{AB} = 6.0 \text{ \AA}$, corresponding to half overlapping DIPBI molecules, which stack with only one PBI wing, each. Analogous patterns emerge with lower density at $d_{AB} = 8.0 \text{ \AA}$ and $d_{AB} = 12.0 \text{ \AA}$, corresponding to the second-nearest and third-nearest neighbours, respectively. The obscure region in the centre around $\alpha \in [30^\circ, 170^\circ]$ and $d_{AB} < 10 \text{ \AA}$ corresponds to physically unrealisable arrangements due to the spatial extension of the unflexible DIPBI core without side chains measuring about $15 \times 15 \times 4 \text{ \AA}^3$. At larger distances of $d_{AB} > 10 \text{ \AA}$, one can also find tilted pair configurations including orthogonally aligned *T*-stacks.

The spots corresponding to DIPBI/DIPBI stacking arrangements are more smeared in the 700 K morphology owing to lateral shift, and the hot spot at $d_{AB} = 4.0 \text{ \AA}$ is reduced in intensity. The number of pairs in the range $d_{AB} = 12.0 - 15.0 \text{ \AA}$ is increased, when compared to 500 K.

The 900 K morphology exhibits a higher tendency for aggregation from $d_{AB} = 4.0 \text{ \AA}$ up to $d_{AB} = 7.0 \text{ \AA}$, where the hot spots are smeared out along the distance axis due to more shear movement along molecular planes at higher temperatures. A reduced number of pairs are found for *T*-stacks in the interval $\alpha \in [50^\circ, 150^\circ]$ and at $d_{AB} = 10 - 14 \text{ \AA}$. All in all, the three density plots detail the presence of stacking aggregates.

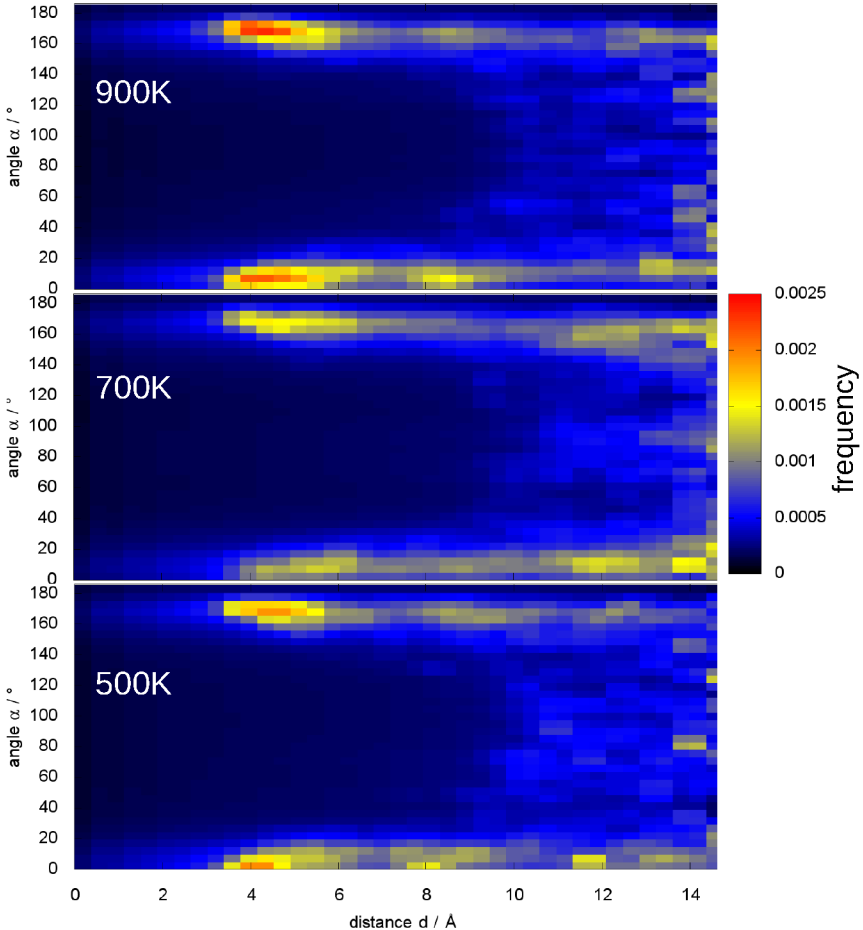


Figure 4.6: Density plots of the distance d_{AB} and the angle α between the normal vectors to the DIPBI planes for three P3HT:DIPBI morphologies at 500 K, 700 K and 900 K.

An alternative measure to characterise the amorphous morphology of blend materials offer radial distribution functions $g(r)$. The function $g(r)$ takes the centres of all DIPBI molecules and the P3HT hopping sites after the segmentation with $\theta_{\text{SCCS}}^{\text{cut}} = 75^\circ$ into account. If we compare the radial distribution functions $g(r)$ of the hopping sites centres, we see that they hardly differ for the three morphologies at 500 K, 700 K and 900 K (Fig. 4.7). The function $g(r)$ reveals a maximum at 3.65 Å to the nearest hopping neighbours, and higher order local maxima at 5.45 Å, 7.25 Å and 9.00 Å.

The radial distribution functions $g(r)$ of the hopping sites centres do not alter significantly for the three morphologies (Fig. 4.7). Also the size distributions of the occurring P3HT segments are similar (Fig. 2.2).

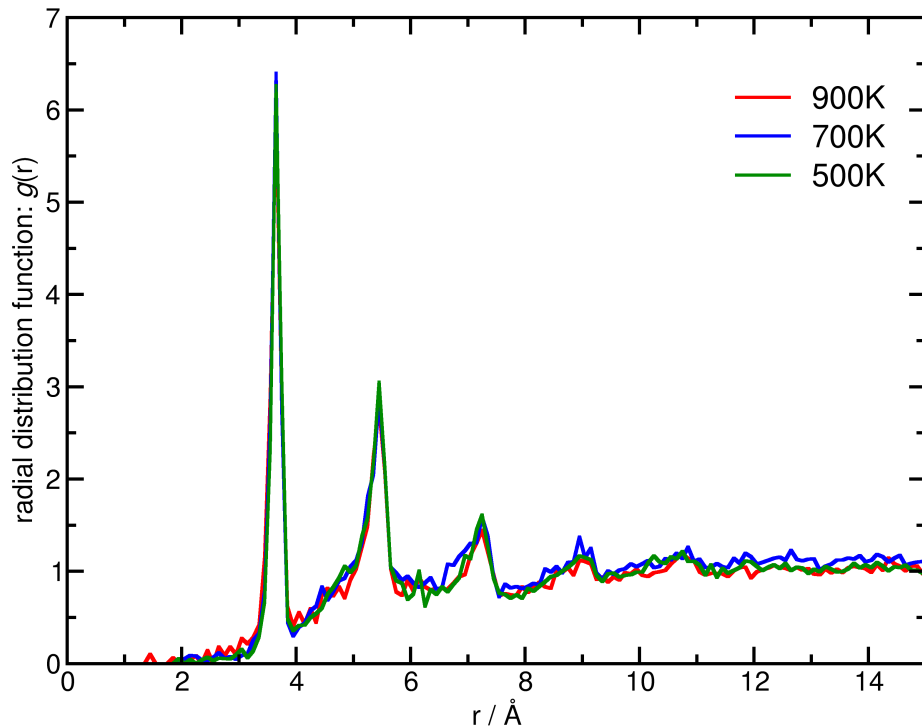


Figure 4.7: Radial distribution function $g(r)$ of the hopping sites centres for the P3HT:DIPBI blend after the polymer chain partitioning with $\theta_{\text{SCCS}}^{\text{cut}} = 75^\circ$ in three different morphologies and CG annealing protocols at 500 K, 700 K and 900 K.

4.1.3.2 Converging the Hole Mobility

In the subsequent section, we check the convergence of physical quantities, e.g. the charge carrier mobility in kMC simulations as a function of different simulation modes. We compare the convergence as a function of the number kMC simulations N_{kmc} , the number of trajectories N_{traj} initialised at the same hopping site and the number of simulation steps N_{steps} . We use a single frame from the P3HT:DIPBI morphology, with a segmentation angle $\theta(\text{SCCS}) = 75^\circ$ with a CDFT/PBE parametrisation for intramolecular charge transfer integrals $|J_{AB}^{\text{int}}$ and energy gap ΔE^{int} . Intermolecular charge transfer $|J_{AB}|$ (DIPRO/PM3) is applied in combination with B3LYP/6-311G**-based reorganization energies λ^{in} and internal site-energy differences ΔE^{in} . Outer-sphere contributions are set to $\lambda^{\text{out}} = 0.0$ eV and $\Delta E^{\text{out}} = 0.0$ eV for simplicity.

As a first step, the convergence of the charge carrier mobility μ (Eq. 260) is checked concerning N_{kmc} . Every simulation is run with $N_{\text{steps}} = 1.0 \times 10^{10}$ steps with a single hole inside the simulation box. Setting the external field in z -direction to a constant value $\mathbf{F}_z^{\text{ext}} = 1.0 \times 10^7 \frac{\text{V}}{\text{m}}$ yields the component μ_z parallel to the field. We start the kMC simulations from different, randomly selected injection sites in the P3HT:DIPBI morphology and observe the convergence of the field-effect mobility μ_z as a function of N_{kmc} (Fig. 4.8). Here, μ_z is evaluated as the running average mobility, and the error bars display the standard deviation σ_{μ_z} . The mobility oscillates for a small number of N_{kmc} and converges to the value $\mu_z = (7.492 \pm 0.028) \times 10^{-3} \text{ cm}^2/\text{Vs}$. The graph confirms that μ_z does not change significantly for $N_{\text{kmc}} \geq 70$, so this value is used as a convergence criterion in the following kMC simulations for a given setup configuration.

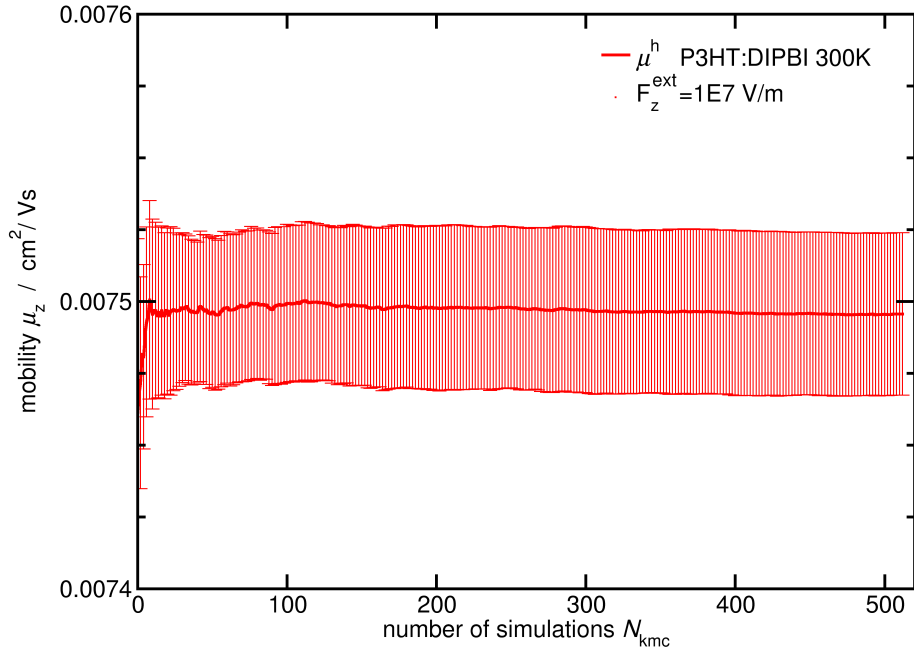


Figure 4.8: Running average of the hole mobility μ_z as a function of the number of kMC simulations $N_{\text{kmc}} = 1$ to 512, including a single charge carrier with intramolecular and intermolecular transport at a fixed external field $\mathbf{F}_z^{\text{ext}} = 1.0 \times 10^7 \frac{\text{V}}{\text{m}}$. Each kMC simulation runs $N_{\text{steps}} = 1.0 \times 10^{10}$. The error bars represent the standard deviation σ_{μ_z} . The converged mobility is $\mu_z = (7.492 \pm 0.028) \times 10^{-3} \text{ cm}^2/\text{Vs}$. The Marcus rate parametrisation includes J_{AB} (DIPRO/PM3) and λ^{in} (B3LYP/6-311G**).

Instead of a random selection of different hopping sites, one can also start from a fixed charge injection site and evaluate a number of different simulations, which are initialised with different random seeds, that hence lead to deviations in the charge carrier trajectories after a few simulation steps. A selection of $N_{\text{traj}}=512$ trajectories is started at a P3HT site inside the P3HT:DIPBI morphology. It leads to a distribution of charge carrier mobilities (Fig. 4.9), which is centred at $\mu_z^h = (7.495 \pm 0.028) \times 10^{-3} \text{ cm}^2/\text{Vs}$. In principle, the simulations, that start from the same origin and different injection points (with the same molecular type) yield the same average result for the hole mobility and also lead to a similar standard deviation for the selected setup. However, there are cases where the energetic landscape is more diversified and rough, and therefore some injection points lead to charge trapping. As a consequence, the sampling of trajectories with distinct starting points is preferred.

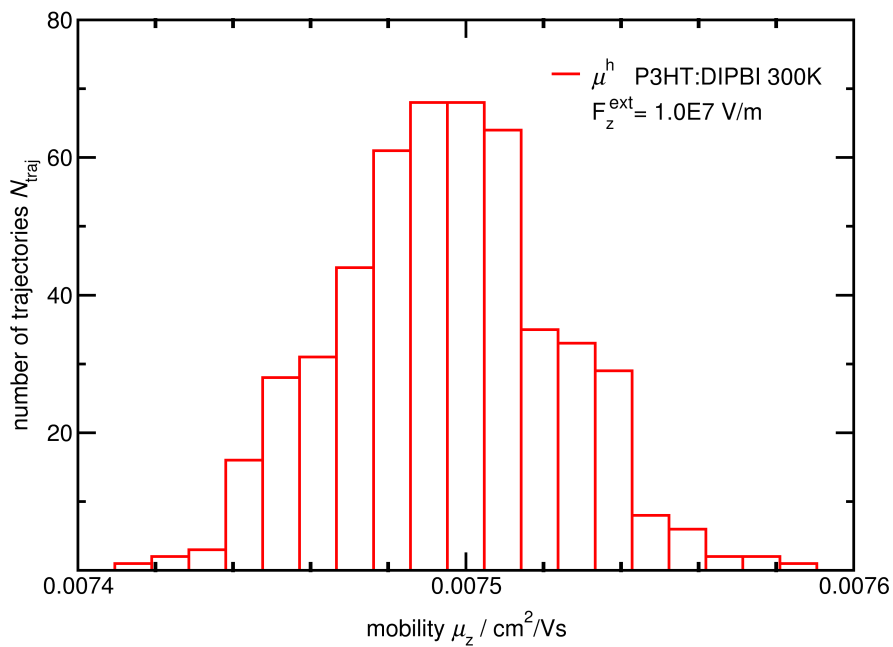


Figure 4.9: Distribution of hole mobilities for $N_{\text{traj}} = 512$ single charge carrier trajectories including intramolecular and intermolecular transport. The holes are injected at the same P3HT hopping site inside the P3HT:DIPBI morphology and the kMC simulations are carried out with different initial random seeds. The external field is set to $\mathbf{F}_z^{\text{ext}} = 1.0 \times 10^7 \text{ V/m}$ and each kMC simulation runs $N_{\text{steps}} = 1.0 \times 10^{10}$ steps. The converged average mobility is $\mu_z^h = (7.495 \pm 0.028) \times 10^{-3} \text{ cm}^2/\text{Vs}$.

Another convergence parameter is the number of kMC steps N_{steps} , which represents the number of charge transitions in a single charge carrier simulation. Note that every single jump is counted in N_{steps} , even if the charge does not proceed in space in a sequence of back and forth jumps between two hopping sites. Such a scenario can take place several hundred times depending on the rate distribution. Starting $N_{\text{kmc}} = 512$ simulations at a set of 512 fixed initial sites and averaging the mobilities after a selected number of N_{steps} , yields convergence of the mobility to $\mu_z = (-7.494 \pm 0.009) \times 10^{-3} \text{ cm}^2/\text{Vs}$ (Fig. 4.10). This value is obtained with $N_{\text{steps}} = 1.0 \times 10^9$ to a relative accuracy of 1/300. The associated error decreases slowly with rising N_{steps} . As the fit function $\sigma_z = aN_{\text{steps}}^b$ yields $a = 2.635 \text{ cm}^2/\text{Vs}$ and $b = -0.497$, we see that σ_z is proportional to $\frac{1}{\sqrt{N_{\text{steps}}}}$ (see inset Fig. 4.10).

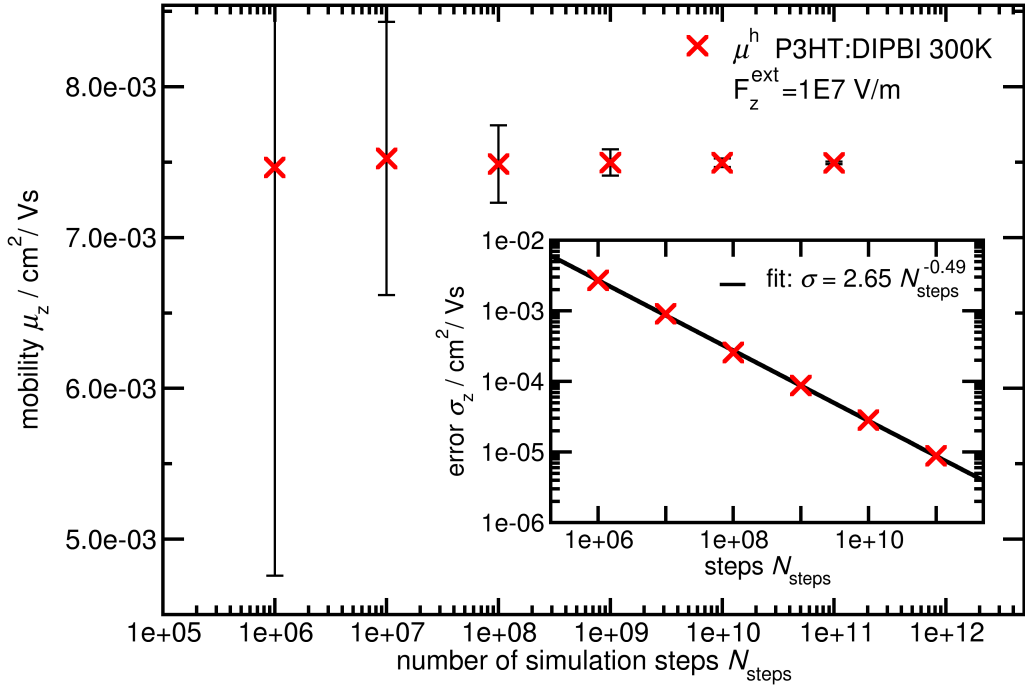


Figure 4.10: Convergence of the average hole mobility μ_z as a function of the kMC steps N_{steps} in single charge carrier simulations. $N_{\text{kmc}} = 512$ trajectories are sampled for $N_{\text{steps}} = 1.0 \times 10^6$ to 1.0×10^{11} with the same initial set of charge injection sites. All kMC simulations include intramolecular and intermolecular transport at a fixed external field $\mathbf{F}_z^{\text{ext}} = 1.0 \times 10^7 \frac{\text{V}}{\text{m}}$. The inset displays the slow decay of the error σ_z , which is proportional to $1/\sqrt{N_{\text{steps}}}$ (fit function).

Figure 4.11 displays the mobility distribution of $N_{\text{kmc}} = 512$ kMC simulations with a distinct maximum numbers steps N_{steps} . The distributions of the mobilities are centred around a single accumulation point. They exhibit a Gaussian shape. The distribution is broad at a $N_{\text{steps}} = 1.0 \times 10^6$ and the width decreases as N_{steps} rises.

Even though we employ intermolecular and intramolecular charge transfer in the blend morphology with mixed domains, we do not see two or more accumulations points in the mobility. This could be caused by the relaxation of the excess charges to distinct, isolated major charge transport channels. Moreover, the overall mobility is independent of the point of injection in the simulation box. In total, with a rising number of kMC steps, one can reduce the statistical error of the simulated charge carrier mobilities, while sampling the same mobility average value for a given configuration. The numerical values for the mean mobility and the standard deviation as a function of the kMC simulation steps N_{steps} are listed in Table A.1.

As a result of the above, we employ $N_{\text{steps}} = 1.0 \times 10^{10}$ kMC simulation steps as a default, because it yields the mobility with sufficient accuracy. However, the magnitude of σ_z , which is achieved with the default settings, crucially depends on the energetic landscape in the system. It can vary significantly, if $\lambda^{\text{out}} \neq 0.0 \text{ eV}$ and $\Delta E^{\text{out}} \neq 0.0 \text{ eV}$ (see Sec. 4.2.2 for comparison).

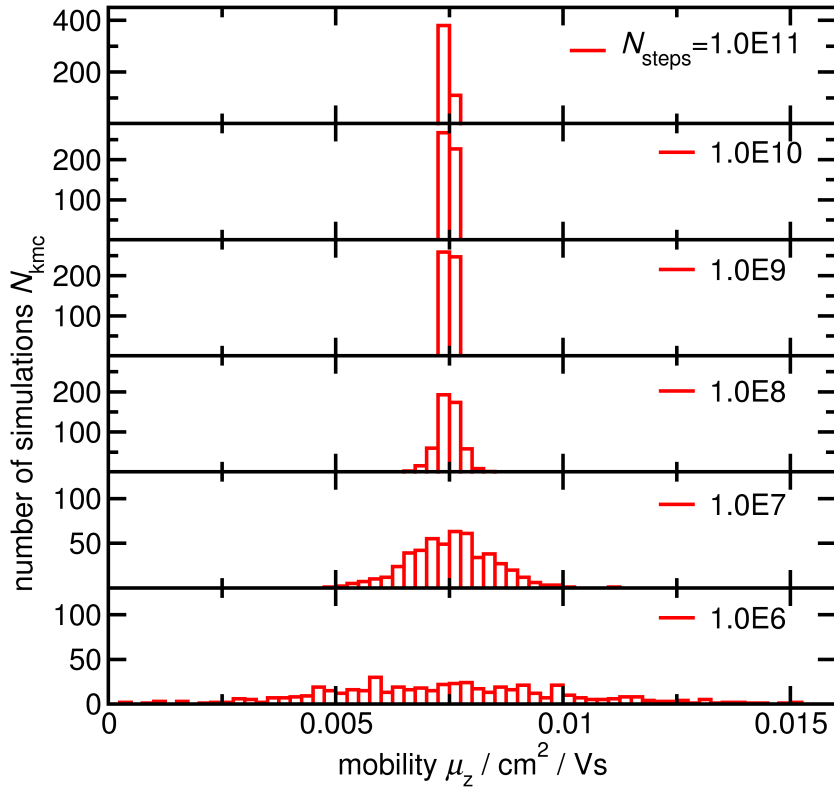


Figure 4.11: Distributions of the hole mobility μ_z as a function of the kMC steps N_{steps} in single charge carrier simulations. $N_{\text{kmc}} = 512$ trajectories are sampled for $N_{\text{steps}} = 1.0 \times 10^6$ to 1.0×10^{11} with the same initial set of charge injection sites. The mobility converges to $\mu_z = (7.494 \pm 0.009) \times 10^{-3} \text{ cm}^2/\text{Vs}$. All kMC simulations include intramolecular and intermolecular hole transport at a fixed external field $\mathbf{F}_z^{\text{ext}} = 1.0 \times 10^7 \frac{\text{V}}{\text{m}}$.

The investigations concerning N_{kmc} , N_{traj} and N_{steps} yield basically the same value for the converged mobility μ_z for the investigated setup.

In an analogous manner, we obtain the other components in the mobility $\mu_x = (5.562 \pm 0.009) \times 10^{-3} \text{ cm}^2/\text{Vs}$ and $\mu_y = (1.714 \pm 0.029) \times 10^{-3} \text{ cm}^2/\text{Vs}$ using $N_{\text{steps}} = 1.0 \times 10^{10}$, $N_{\text{kmc}} = 70$ at an external field $\mathbf{F}_x^{\text{ext}} = 1.0 \times 10^7 \frac{\text{V}}{\text{m}}$ and $\mathbf{F}_y^{\text{ext}} = 1.0 \times 10^7 \frac{\text{V}}{\text{m}}$, respectively. They combine with μ_z to the total mobility $\bar{\mu}_{\text{tot}}^{\text{h}} = (9.49 \pm 0.04) \times 10^{-3} \text{ cm}^2/\text{Vs}$.

4.1.3.3 Sampling the Hole Mobility in Multiple Morphologies

The morphology of a BHJ-OSC can change over time t , as thermal fluctuations can alter the relative orientation of molecules and hence influence the charge carrier dynamics. Especially, the dynamics along the polymer backbone can alter the relative orientation of thiophene units, which we take into account in our model by the adaption of the polymer chain partitioning. Hence, the number and location of the hopping sites change as well as the thiophene segment length n .

In previous investigations, we always focused on the charge carrier mobility μ for a single, static snapshot of the trajectory from MD simulations. We usually represent the morphology on an atomistic level. In the following, we call such a snapshot of the morphology with an atomistic, frozen configuration of nuclear coordinates a frame and see how sampling a number of different frames N_{frames} affects the total charge carrier mobility.

The P3HT:DIPBI frames are generated as follows. We start with the P3HT:DIPBI morphology, which was obtained in CG simulations at an annealing temperature of $T = 500$ K [64] and heat the system in an atomistic MD simulation to $T = 900$ K for $t = 6$ ns, using a velocity rescale thermostat [180] and a Parrinello-Rahman barostat [271] in a NPT simulation with a constant pressure of $p = 1$ bar and a time step $\Delta t = 1$ fs. We extract a snapshot from the trajectory after every time interval $\Delta t = 0.5$ ns and cool the system to $T = 300$ K in a subsequent run for 0.5 ns in each case. All 12 obtained frames yield similar extensions of the orthorhombic unit cell ($16.2 \times 31.5 \times 17.1$ nm 3).

We evaluate the hole mobilities for every frame using two different types of setups μ^α and μ^β . In both cases, we use intermolecular charge transfer integrals J_{AB} (DIPRO/PM3) and scale the results to CDFT. Likewise, the CDFT data is employed for intramolecular charge transfer (Sec. 3.1.7). We determine the outer-sphere contributions ΔE^{out} and λ^{out} without the segmentation of the P3HT chains $n = 32$. The hole mobilities μ^h in different P3HT:DIPBI frames are compared in Figure 4.12 as a function of the annealing time t .

If we evaluate the hole mobilities μ^α , using a randomised charge injection, we find large fluctuations in μ^α as a function of t that vary about four orders of magnitude. We obtain a maximum mobility of $\mu_{\max}^\alpha = (2.15 \pm 4.12) \times 10^{-7}$ cm 2 /Vs at $t = 4$ ns. The question arises whether the large fluctuations are prone to morphological changes or just an artefact of different sampling schemes.

In turn, when evaluating μ^β , we maintain the set of P3HT polymer chains for initial charge injection when the underlying morphology changes with time t . The hole mobilities μ^β also fluctuate as a function of t . The trend of μ^β roughly coincides with the one in μ^α , taking into account the high standard deviations σ_μ . However, the amplitude in the fluctuations in μ^β is reduced compared to μ^α . The maximum value μ_{\max}^β is also found at $t = 4$ ns. In total, the average hole mobilities for all $N_{\text{frames}} = 12$ frames yields $\bar{\mu}^\alpha = (2.06 \pm 4.53) \times 10^{-8}$ cm 2 /Vs and a smaller value for $\bar{\mu}^\beta = (1.88 \pm 10.62) \times 10^{-9}$ cm 2 /Vs. For the similarities in the fluctuations of μ^α and μ^β , we assume morphological changes to cause alterations in μ in the course of t .

To test this hypothesis, we have a look at characteristic properties for different frames (Fig. 4.13). First, we determine the average planarity descriptor P^\flat (Eq. 279), taking all P3HT chains with $n = 32$ in each frame into account. The planarity descriptor remains basically at the same level for all frames. When taking the average for all $N_{\text{frames}} = 12$ frames, we obtain a value $\bar{P}^\flat = 6.82 \pm 0.89$. The planarity descriptor \bar{P}^\flat is significantly reduced compared to pure P3HT and slightly smaller when compared to the morphologies with annealing temperatures at 500 K, 700 K and 900 K (Fig. 4.5).

The outer-sphere reorganization energies also yield similar distributions for all frames, and the average remains constant. They are determined without a segmentation of the thiophene chains and yield an average $\bar{\lambda}^{\text{out}} = (0.048 \pm 0.019)$ eV. The same holds for the outer-sphere contributions to the site-energy E_i^{out} , that yield an average value $\bar{E}_i^{\text{out}} = (-0.040 \pm 0.124)$ eV. It yields the highest value at $t = 1.5$ ns. In the same manner, we evaluate the distributions of the charge transfer integrals and obtain the average $|\bar{J}_{AB}|$ (DIPRO/PM3). Every frame gives rise to $N_{\text{pairs}} \approx 7.5 \times 10^4$ intermolecular charge transfer pairs. They lead to a total average $|\bar{J}_{AB}| = (0.031 \pm 0.107)$ eV. Both the form of the distributions of $|J_{AB}^h|$ and the averages do not exhibit significant deviations over time.

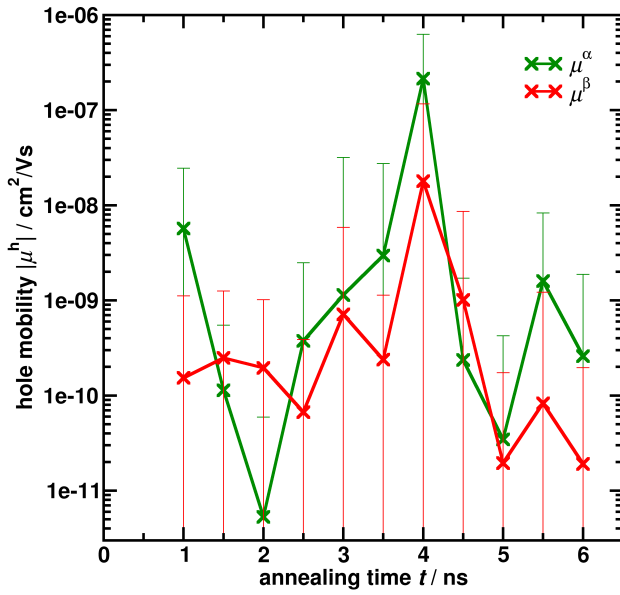


Figure 4.12: Hole mobilities in different P3HT:DIPBI frames as a function of the annealing time t . The mobilities are evaluated for two different types of setups μ^α and μ^β . Both use J_{AB} (DIPRO/PM3) scaled to CDFT charge transfer integrals for intermolecular charge transfer and CDFT for intramolecular charge transfer. The outer-sphere contributions ΔE^{out} and λ^{out} are evaluated without segmentation of the P3HT chains $n = 32$. Random charge insertion is applied in μ^α and μ^β the initial ensemble of selected hole injection sites remains at the same set of P3HT chains for all morphologies.

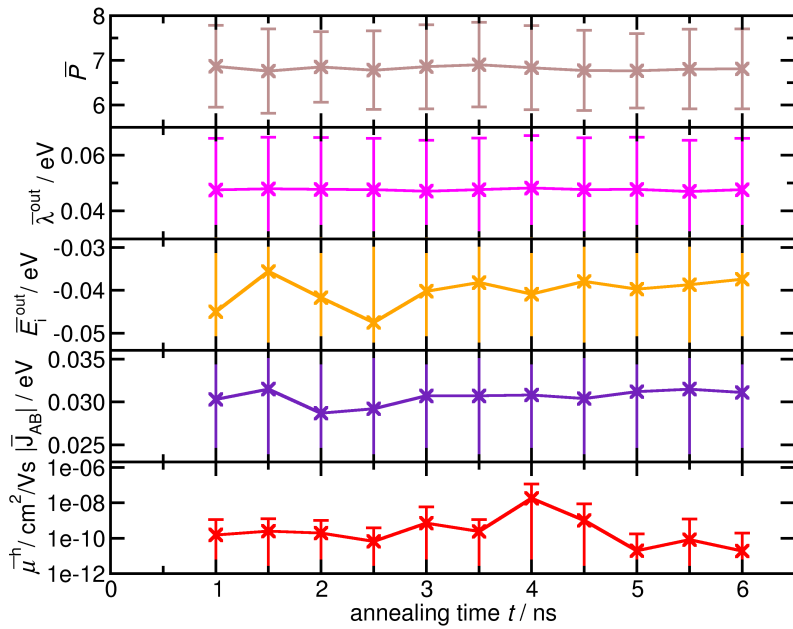


Figure 4.13: Dependence of properties in distinct P3HT:DIPBI frames as a function of the annealing time t . Averaged values of the planarity descriptor \bar{P}^b , outer-sphere contributions \bar{E}_i^{out} and $\bar{\lambda}^{\text{out}}$ without segmentation of the P3HT chains $n = 32$, intermolecular charges transfer integrals $|\bar{J}_{AB}|$ DIPRO/PM3 for pairs including the $N^{\text{NN}} = 12$ nearest neighbours of each hopping site are compared to the hole mobility $\bar{\mu}^h$.

In total, the averages of selected key properties \bar{P}^b , $\bar{\lambda}^{\text{out}}$, \bar{E}_i^{out} and $|\bar{J}_{AB}|$ do not reflect the same trend as the hole mobility μ^h . They do not change significantly with t . At this stage, the origin of fluctuations in the hole mobility μ^h remains unclear. However, averaging the mobility for different frames N_{frames} is an appealing strategy to sample charge carrier pathways in different structural arrangements, provided that the selected frames are structurally uncorrelated.

4.1.3.4 Comparing Simulation Approaches for Hole Mobilities

In the following, we discuss kMC results obtained with different approximations and morphologies. We start with kMC simulations performed for a single time frame from the morphology at 500 K with charge transfer integrals $|J_{AB}|$ calculated using the CDFT/PBE and unscaled DIPRO/PM3 approaches for intramolecular and intermolecular hops, respectively, and internal reorganization energies λ^{in} computed at the DFT/B3LYP/6-311G* level. If we set all outer-sphere contributions to zero, we obtain a rather high charge carrier mobility of $\mu_{\text{tot}}^h = (6.02 \pm 0.05) \times 10^{-3} \text{ cm}^2/\text{Vs}$. The inclusion of outer-sphere reorganization energy contributions λ^{out} for a whole P3HT 32mer results in a reduction of the charge carrier mobility by four orders of magnitude to $(2.60 \pm 0.06) \times 10^{-7} \text{ cm}^2/\text{Vs}$.

Additional incorporation of site-energy differences ΔE^{out} contributions for a whole P3HT 32mer (Sec. A.19) does not alter the mobility significantly, yielding a value of $(3.07 \pm 0.08) \times 10^{-7} \text{ cm}^2/\text{Vs}$. Analogous simulations for the morphologies obtained at 700 K and 900 K give mobilities of $\mu_{\text{tot}}^h = (2.58 \pm 0.14) \times 10^{-7} \text{ cm}^2/\text{Vs}$ and $(5.27 \pm 0.15) \times 10^{-8} \text{ cm}^2/\text{Vs}$, respectively. These findings correlate with the increasing degree of order found with decreasing annealing temperature [64].

Scaling the DIPRO/PM3 intermolecular transfer integrals to the CDFT reference data dramatically raises the hole mobility to $(8.41 \pm 0.07) \times 10^{-3} \text{ cm}^2/\text{Vs}$ for the 500 K morphology – an increase by four orders of magnitude including outer-sphere contributions for entire polymer chains (see Sec. A.1.8).

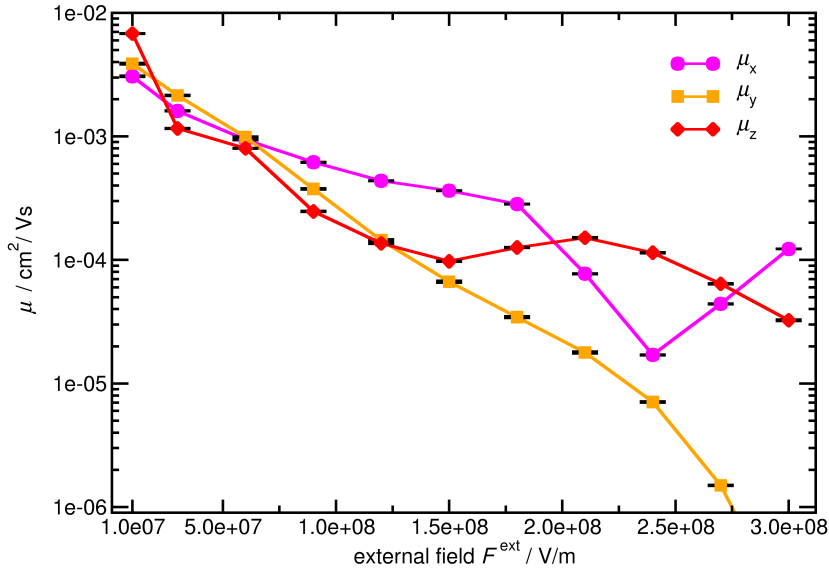


Figure 4.14: Charge carrier mobility μ_i ($i \in x, y, z$) in P3HT:DIPBI as a function of the external field strength F_i^{ext} in i -direction. Charge transfer integrals $|J_{AB}|$ were obtained from DIPRO/PM3 scaled to CDFT.

Hole Mobility and External Field Dependence The influence of the external field strength on the charge carrier mobility was investigated in the interval $F_i^{\text{ext}} \in [1.0 \times 10^7, 3.0 \times 10^8] \text{ V/m}$ (Fig. 4.14). Overall, an inverse field dependence can be seen, i.e. the mobility decreases with increasing external field by up to four orders of magnitude in this interval. It can also be seen that charge transport is practically isotropic. The curves for μ_x , μ_y , and μ_z appear to be particularly close together at low external fields, but this is owed to the logarithmic scale.

To our knowledge, no experimental data for charge carrier mobilities in P3HT:DIPBI blends are available so far. Our simulations suggest, however, that the mobility in the blend is considerably enhanced compared to amorphous P3HT (see above).

Hole Mobility and Temperature Dependence As the charge transfer rates vary as a function of temperature T , also the simulated hole mobility μ^h depends on T (Fig. 4.15). The mobility rises with increasing T , and we employ the curve-fitting [248] to the temperature dependence (Eq. 264) to interpolate the mobility in the range from $T = 300 \text{ K}$ to 5000 K . Looking at the temperature dependence in precise terms, it is only valid in one dimension. Hence, we employ the curve-fitting to single components of the field-effect mobility μ_x , μ_y and μ_z instead of to the total hole mobility μ^{tot} . The fits yield the material constants $\mu_x^0 = 1.12 \text{ cm}^2/\text{Vs}$, $\chi_x = 0.583 \text{ K}$, $\zeta_x = 0.573 \text{ K}$ for μ_x , $\mu_y^0 = 1.47 \text{ cm}^2/\text{Vs}$, $\chi_y = 0.656 \text{ K}$, $\zeta_y = 0.839 \text{ K}$ for μ_y as well as $\mu_z^0 = 1.73 \text{ cm}^2/\text{Vs}$, $\chi_z = 0.583 \text{ K}$ and $\zeta_z = 1.57 \text{ K}$ for μ_z . The high correlation coefficients $R_x = 0.994$, $R_y = 0.981$ and $R_z = 0.978$ reflect the validity of the temperature dependence (Eq. 264) also in the P3HT:DIPBI morphology.

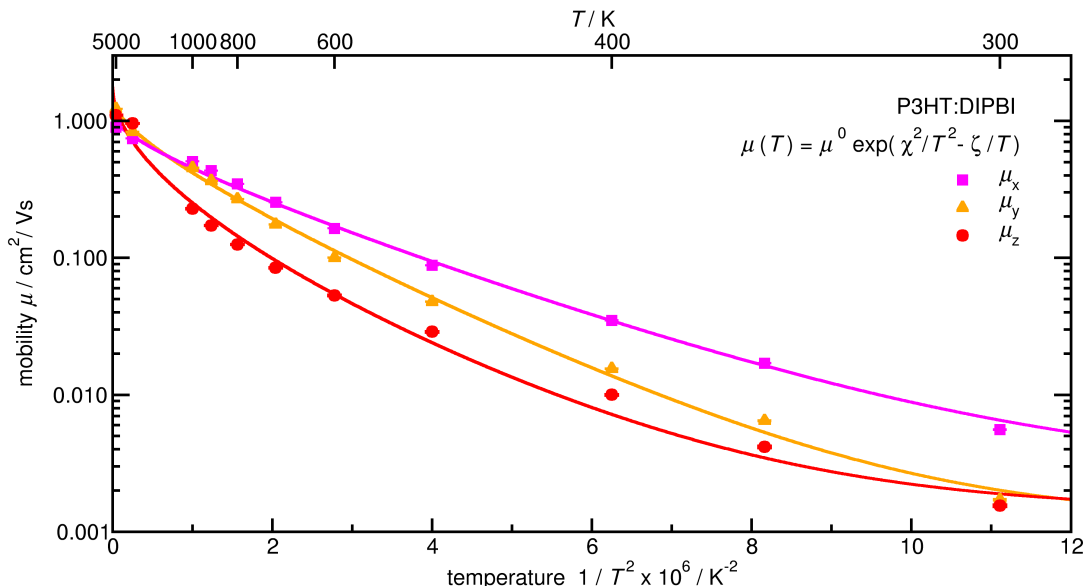


Figure 4.15: Temperature dependence of the hole mobility μ^h in P3HT:DIPBI blend at a constant external field $|F^{\text{ext}}| = 1.0 \times 10^7 \text{ V/m}$. The points correspond to kMC results and the curve-fittings to equation (Eq. 264) detail the temperature T dependence of single components in the field-effect mobility μ_x , μ_y and μ_z .

4.1.3.5 Site Occupation

Figure 4.16 displays the 10% most occupied hopping sites in the P3HT:DIPBI morphology and their respective average occupations. It indicates that segments with high occupancy are irregularly distributed within the morphology. Note that the occupation numbers vary over many orders of magnitude, even within the top 10%. The site with the highest occupation is a terminal P3HT chain segment with $n = 6$ and an occupation probability of $p = 0.28\%$. As illustrated by Fig. 4.16, hole transport occurs predominantly within the P3HT network. Of the top 10% most populated sites, about 5% are DIPBIs (4.16, top) and 95% are P3HTs (4.16, bottom). The DIPBI molecules are evenly scattered inside the simulation box and do not emerge in large clusters or networks, the maximum number of molecules in an aggregate being three. In addition, the DIPBIs exhibit only low to medium occupation numbers. The P3HT molecules, on the other hand, clearly form a three dimensional network inside the simulation box representing highly efficient charge transport channels which are separated from each other by vast void spaces. In fact, 16% of all DIPBI and 7% of P3HT hopping sites are never visited at all in the simulations. The picture emerging from the above population analysis, that hole transport takes place mainly in the P3HT subsystem, is further underlined by a closer look at the number of hops occurring between different types of sites. It turns out that 99.8% of all hops occur from a P3HT segment to another P3HT segment, which differentiate into 6.3% intramolecular and 93.7% intermolecular jumps. Only 0.1% of all hole jumps occur from one DIPBI to another DIPBI, a small portion of $8.09 \times 10^{-4}\%$ are transitions from DIPBI to P3HT and a slightly lower amount jumps in opposite direction, which exclusively arise from segments with $n \leq 3$.

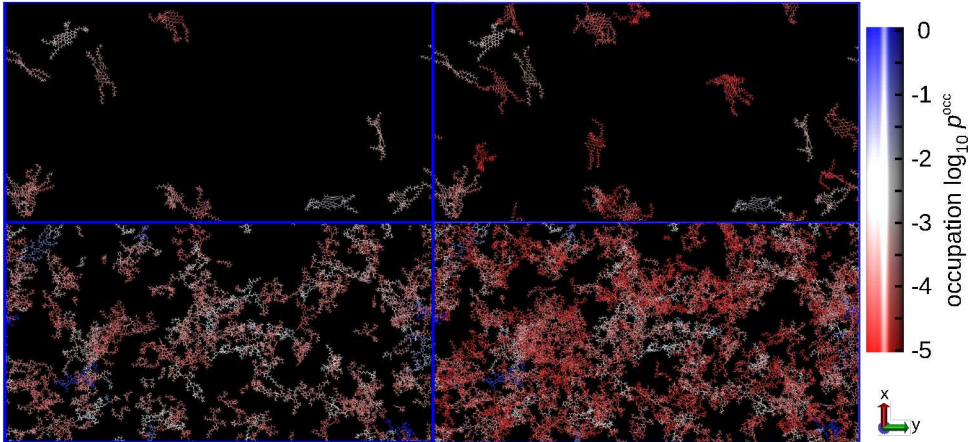


Figure 4.16: Hopping sites with the 5% (left) and 10% (right) highest occupation in the P3HT:DIPBI morphology from kMC simulations with holes at an external field $F_y^{\text{ext}} = 1.0 \times 10^7 \frac{\text{V}}{\text{m}}$. Upper panel: DIPBI, lower panel: P3HT. The occupation numbers are averages over 72 charge carrier trajectories.

In addition to locating the sites with the highest occupations, we have also calculated the overall average occupation numbers \bar{p}^h for DIPBI and different segment lengths of P3HT. As can be seen from Figure 4.17 the average occupation of DIPBI is far lower than any P3HT value, in line with the above observations. Figure 4.17 also reveals a tendency for rising occupations with increasing segment length n , which goes hand in hand with an increased average resting time (Fig. 4.18) and an increased delocalisation of the excess charge.

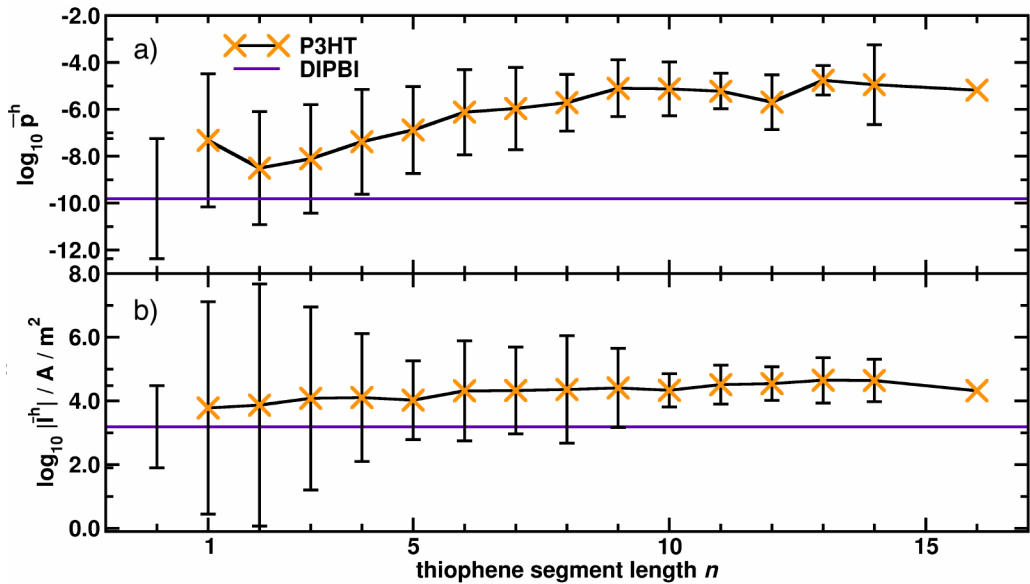


Figure 4.17: Decadic logarithm of average hole occupation numbers $\log_{10} \bar{p}^h$ and average local current per hopping site $|\bar{I}^h|$ for hole transport as a function of the thiophene chain length n of a conjugated segment in the P3HT:DIPBI morphology from kMC simulations at an external field $F_y^{\text{ext}} = 1.0 \times 10^7 \frac{\text{V}}{\text{m}}$.

The average escape Marcus rate \bar{k}^{esc} (Eq. 250) decays as a function of the thiophene segment length n (Fig. 4.18). The average hole escape rate from a DIPBI molecule exceeds the value of P3HT for hole transfer, which is in line with the expected donor/acceptor character of P3HT and DIPBI. Note the logarithmic scale and the large standard deviations. The outliers at $n = 14$ and 16 are attributed to missing statistics and local energetic disorder.

As the average resting time t^r is the inverse of the escape rate \bar{k}^{esc} , one finds an increasing resting time for longer thiophene segments. Accordingly, the average resting time for holes is shorter on DIPBI molecules than on P3HT segments.

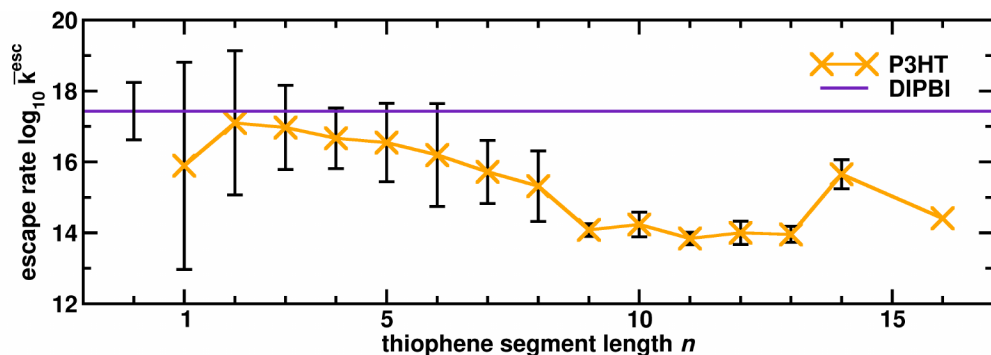


Figure 4.18: Decadic logarithm of the average escape Marcus rate $\log_{10} \bar{k}^{\text{esc}}$ from hopping sites as a function of the thiophene segment length n of a conjugated segment in the P3HT:DIPBI morphology. The \bar{k}^{esc} for hole transfer include intermolecular and intramolecular transitions in P3HT. The average value for DIPBI is shown for comparison.

4.1.3.6 Current and Low Resistance Pathways

The average local current per hopping site $|\bar{I}^h|$ for hole transport (Eq. 266) is depicted in the bottom panel of Figure 4.17 as a function of the P3HT segment length n . The overall trend is that $|\bar{I}|$ increases with n , being larger by one order of magnitude for the longest segments compared to the shortest. As the hole occupation numbers are low for DIPBI molecules (see above), the contribution of DIPBI to the total current is also low.

The regions of high average local current are illustrated in Figure 4.19. As the isosurface with $I = 1.12 \text{ A/m}^2$ (red tubes) shows, there exists a network of current tracks along which hole transport predominately occurs. Among the hopping sites with the highest 10% local current contributions to the total current, the vast majority (94.9%) are P3HT segments and only about 5.1% DIPBI molecules.

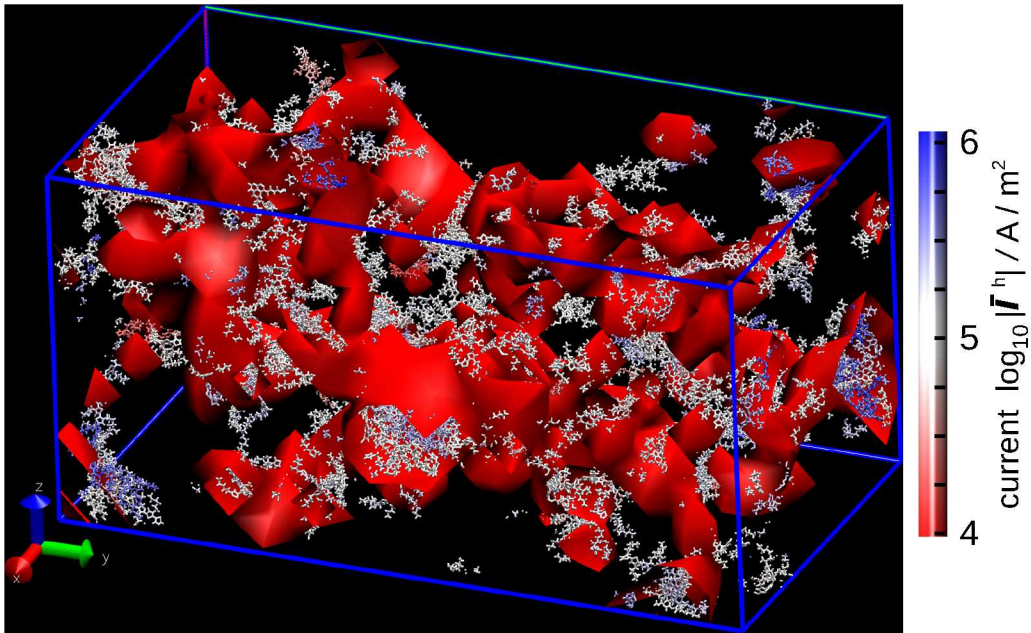


Figure 4.19: Molecules with the highest 10% local current contribution $\log_{10} |\bar{I}^h|$ to the total current (colour-coded) based on kMC simulations of hole transport in P3HT:DIPBI morphology. The simulation box includes the isodensity surface for the local hole current at $I = 1.12 \text{ A/m}^2$ (red tubes).

The pathway of lowest resistance for the charge carriers to cross the simulation box is evaluated using Dijkstra's algorithm [73]. For this purpose, we define the external voltage between two hopping sites i and j as $U_{ij} = \mathbf{F}^{\text{ext}} \cdot \mathbf{d}_{ij}$ and evaluate the current \mathbf{I}_{ij} on the basis of the occupation numbers p_i^{occ} and charge transfer rates k_{ji} and thus determine the local resistance

$$|R_{ij}^{\text{loc}}| = \frac{|U_{ij}|}{|\mathbf{I}_{ij}|} = \frac{|\mathbf{F}^{\text{ext}} \cdot \mathbf{d}_{ij}|}{|e(p_i^{\text{occ}}k_{ij} - p_j^{\text{occ}}k_{ji})\mathbf{e}_{ij}|}. \quad (284)$$

where $\mathbf{e}_{ij} = \mathbf{d}_{ij}/d_{ij}$ is the unit vector connecting the two sites. This way we have transformed the network of local currents $|\mathbf{I}_{ij}|$ to one of local resistances $|R_{ij}^{\text{loc}}|$ between nodes. To analyze the charge carrier pathways between the two electrodes, we follow the charge carrier movement between two narrow slabs perpendicular to the field at opposite ends of

the simulation cell, which we denote as start and end zones. The start zone with a width d_{zone} includes all hopping site centers with $d_l^{\text{COM}} < d_l^{\text{zone}}$ ($l = x, y, z$), while the end zone is obtained by shifting the start zone by the box length d_l^{box} thus extending the box in field direction l by d_{zone} . In other words, we follow the charge carriers until they have travelled the entire length of the box in l -direction. For every hopping site in the start zone, the Dijkstra algorithm is applied to obtain the pathway of lowest resistance $R^{\text{tot}} = \sum_{\text{path}} |R_{ij}^{\text{loc}}|$ for reaching the end zone. This procedure ensures that the minimal resistance pathway crosses the box in direction of the external field.

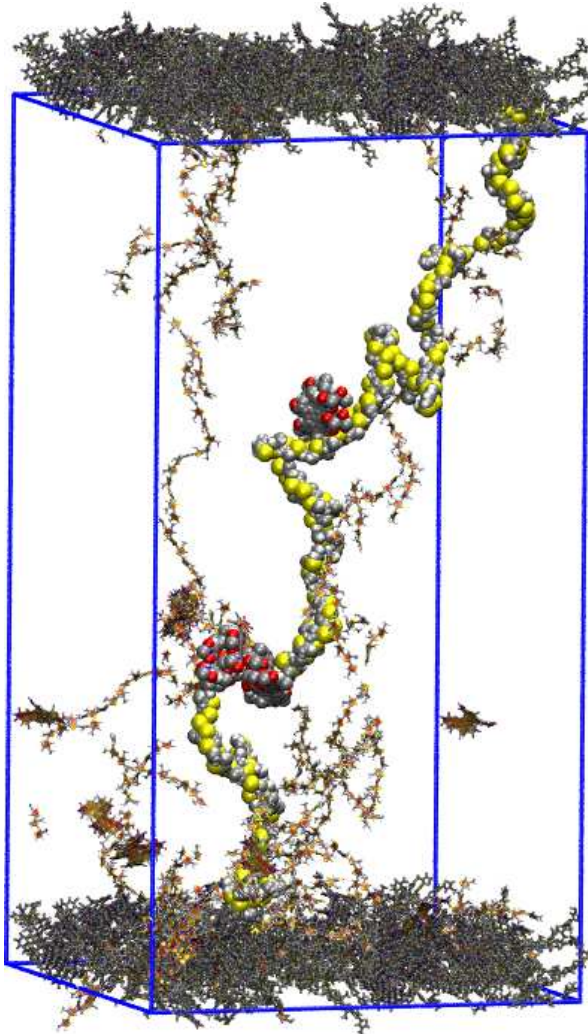


Figure 4.20: Charge carrier pathways with minimal resistance in P3HT:DIPBI morphology based on Dijkstra algorithm. The pathways are determined for every molecule in the start zone (black, below) to those in the end zone (black, above). The molecules, which belong to the pathways, are depicted in the paper chain representation (orange), where the one with the lowest R^{tot} is depicted in VdW representation.

Choosing a thickness of $d_y^{\text{zone}} = 15 \text{ \AA}$, we have 360 hopping sites in the start zone. Figure 4.20 displays 15 representative minimum resistance pathways with different starting points giving rise to three main branches crossing the simulation box with the lowest R^{tot} values (see Fig. A.21 for the distribution of $\log_{10} R^{\text{tot}}$).

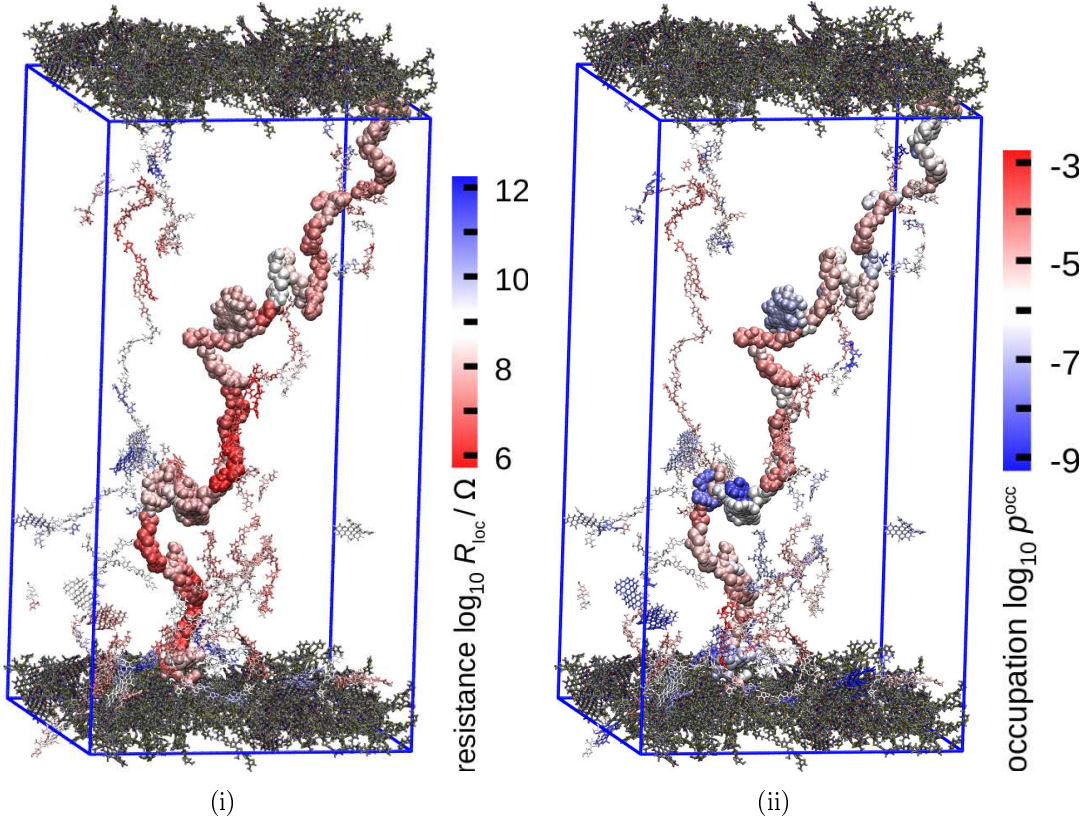


Figure 4.21: Hole transport pathways with small electronic resistance based on Marcus hole transfer rates using the Dijkstra algorithm. (a) Hole transport pathways with (color-coded) local resistance $\log_{10} R^{\text{loc}}$ and (b) the occupation numbers $\log_{10} p^{\text{occ}}$.

The pathways include several stretched thiophene chains that are predominantly oriented parallel to the external field direction y . The pathway with the smallest R^{tot} consist of 196 thiophene units and nine DIPBI molecules involving 32% intramolecular transitions and 55% intermolecular transitions within the same domain, and 12% D/A or A/D transitions. It traverses five DIPBI molecules that are connected by a π -stacking motive with lateral shifts. Also the parallel alignment of thiophene chains facilitates charge transport.

We can correlate these structural features of the pathways to the local resistance $\log_{10} R^{\text{loc}}$ (Fig. 4.21,i). The pathway exhibits small resistance along linear sections and larger values at winding sections with predominantly intermolecular transitions at the interfaces. Taking the average resistance of all low resistance pathways yields $\log_{10} R^{\text{tot}} = (10.7 \pm 1.1) \Omega$ with a minimum resistance $\log_{10} R_{\text{min}}^{\text{tot}} = 9.7 \Omega$. Note that the lowest possible resistance of a molecule is $\pi\hbar/e^2 = 12.9 \text{ k}\Omega$ [386]. Experimental investigations find a linear relationship between the molecular length and resistance in oligothiophenes chain length $n > 11$ at the order $\log_{10} R = 8 \text{ to } 10 \Omega$ [387, 388], which coincides with our findings.

The DIPBI molecules exhibit smaller occupation numbers along the pathway compared to those found on P3HT segments especially high p^{occ} at longer chains, which coincides with the findings depicted in Fig. (4.17,i). Overall, combinations of intramolecular and intermolecular transitions promote efficient hole transport in P3HT:DIPBI morphology.

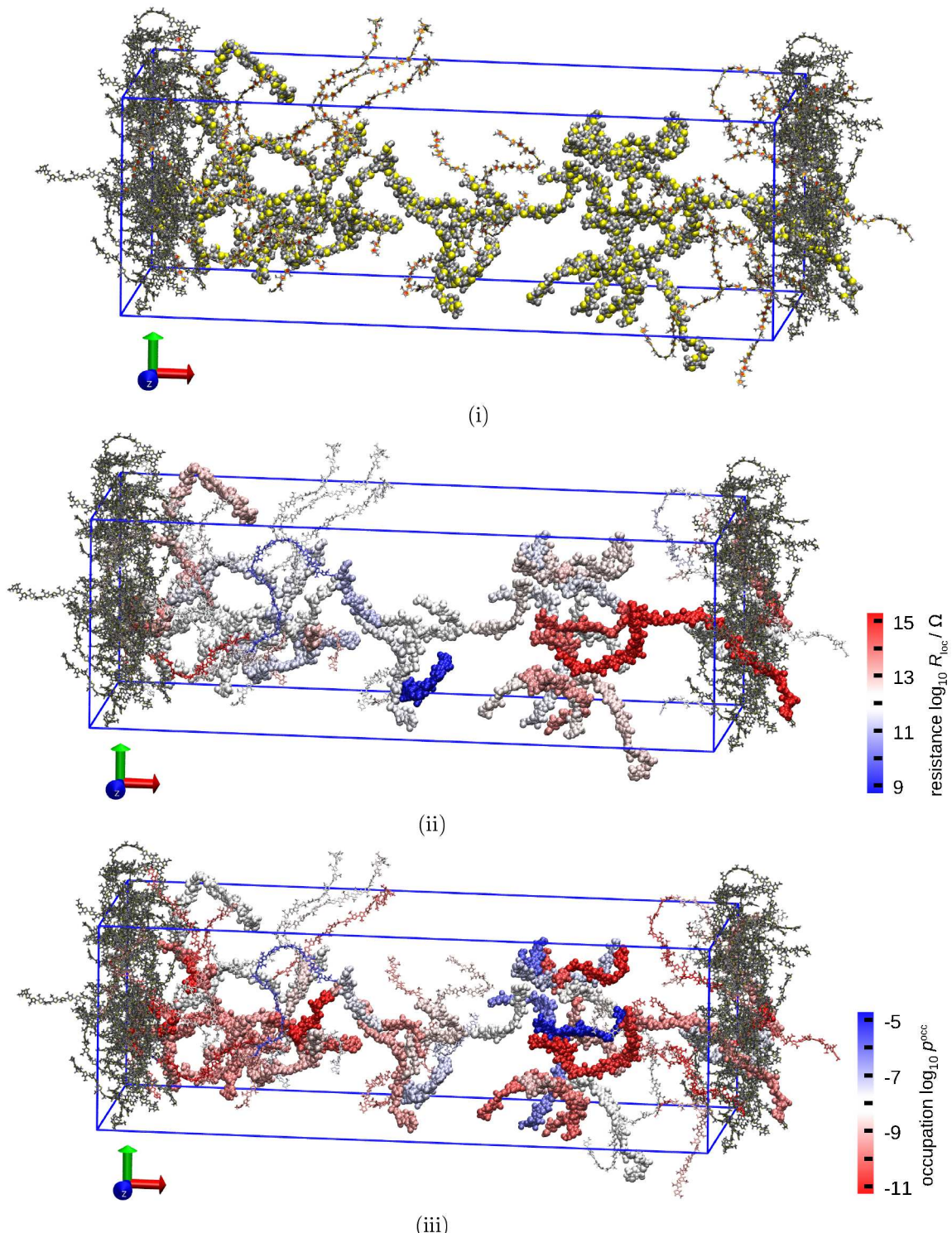


Figure 4.22: Hole transport pathways with small electronic resistance in amorphous P3HT based on Marcus hole transfer rates using the Dijkstra algorithm. (i) The pathways are determined for every molecule in the start zone (black, left) to those in the end zone (black, right). The molecules, which belong to the pathways are depicted in the paper chain representation (orange), where the one with the lowest R^{tot} is depicted in VdW representation. (ii) Hole transport pathways with (color-coded) local resistance $\log_{10} R_{loc}$ and (iii) the occupation numbers $\log_{10} p_{occ}$.

In an analogous analysis for pure P3HT (Fig. 4.22), we obtain a total of 68 hopping sites in the start zone at a thickness $d_x^{\text{zone}} = 15 \text{ \AA}$. We show the 8 pathways with low total resistance $\log_{10} R^{\text{tot}}$ in the P3HT morphology (Fig. 4.22,i). The pathway of lowest local resistance comprises winding chains with mostly planar segments (Fig. 4.22,ii). It consists of 32% intrachain transitions and 67% interchain transitions.

Taking the average resistance of all low resistance pathways, we get $\log_{10} R^{\text{tot}} = (16.4 \pm 0.9) \Omega$ with a minimum resistance $\log_{10} R_{\min}^{\text{tot}} = 14.9 \Omega$. These values exceed those in P3HT:DIPBI consistent with the trend towards larger simulated mobilities in the blend material. It is noticeable that in pure P3HT, the path of lowest resistance contains predominantly long segments with an average chain length of $\bar{n} = 20.1 \pm 8.0$. This exceeds the value of $\bar{n} = 4.7 \pm 2.5$ in the blend.

Finally, the analysis of fast hole transport pathways provides a visualisation of long-held hypotheses about charge transport in opaque morphologies, as it provides a direct correlation of local resistances or occupancies along the pathway with the underlying amorphous polymer structure and aggregation patterns of small molecules.

4.1.3.7 Rate Distributions in the Blend Morphology

In this section, we focus on the predicted direction of hole and electron transfer rates in the amorphous P3HT:DIPBI morphology. We compare the rate distributions for Marcus, Jortner and Weiss-Dorsey charge transfer rates. In particular, we consider the donor/acceptor interface, where we expect an electron transfer from the electron donor P3HT to the electron acceptor DIPBI. In turn, we expect the predominant transfer in the opposite direction for holes.

We compare the rate distributions for hole and electron transfer and take into account all transitions for charge transfer pairs N_{pairs} (Fig. 4.23). The transfer distributions are similar for holes and electrons, apart from the fact that some Jortner rates are higher for electrons ($k^e > 1.0 \times 10^{20} \text{ s}^{-1}$). Comparing the different rate types, we see that the Jortner rates give on average the highest rates with the narrowest distributions. Both Marcus and Weiss-Dorsey rates yield broader distributions than Jortner rates, and the Marcus rates in particular are shifted to lower values.

Comparing the intramolecular charge transfer rates for transitions between P3HT segments (Fig. 4.24), there is a trend towards higher values for electron transfer rates compared to hole transfer rates. All three different rate types exhibit this feature. Some intramolecular Jortner rates overestimate charge transfer, yielding rates in the range of 10^{17} s^{-1} to 10^{21} s^{-1} . This feature of Jortner rates is also known in literature [389], as the Levich-Jortner theory is known to overestimate the charge carrier mobilities strongly and as it shows larger deviations from the experimental results than those obtained with the Marcus theory [389]. The latter contains larger approximations by treating all vibrational modes classically.

It has been demonstrated that this approximation leads to a considerable overestimation of the significance of the high-frequency molecular vibrations to the molecular reorganization upon charge transfer, which lowers the hopping rates. As a result, some studies claim that the Marcus theory fits (some) experimental data better than the Levich-Jortner theory due to error cancellation [389]. However, if we want to describe charge transfer at the donor/acceptor interface, the situation is more complicated.

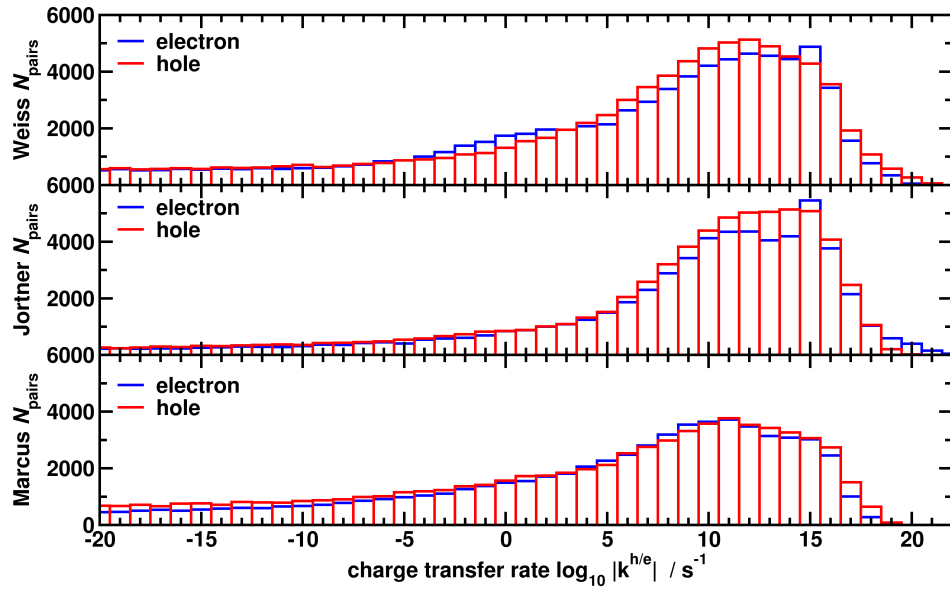


Figure 4.23: Charge transfer rate distributions for all transitions in a P3HT:DIPBI morphology at 500 K with Weiss-Dorsey rates (i), Jortner rates (ii) and Marcus rates (iii) for hole (red) and electron transfer (blue). The rates are evaluated for the following parametrisation including scaled $|J_{AB}|$ PM3 to CDFT, $|\mathbf{F}_z^{\text{ext}}| = 1.0 \times 10^7 \frac{\text{V}}{\text{m}}$, λ^{in} , ΔE^{in} (B3LYP/6-311G*), $T = 300 \text{ K}$.

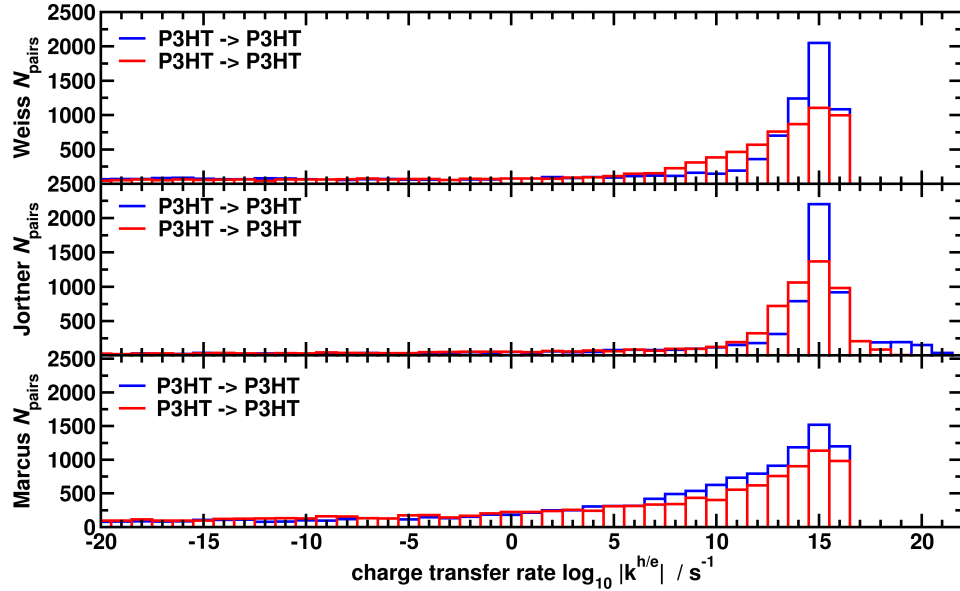


Figure 4.24: Charge transfer rate distributions for intramolecular $\text{P3HT} \leftrightarrow \text{P3HT}$ transitions in a P3HT:DIPBI morphology at 500 K with Weiss-Dorsey rates (i), Jortner rates (ii) and Marcus rates (iii) for hole transfer (red) and electron transfer (blue). All rate types are evaluated using the following parametrisation including CDFT-based charge transfer integrals $|J_{AB}|$ in the ($n_A = 1 \& n_B = 1$) approximation (Fig. 3.21), $|\mathbf{F}_z^{\text{ext}}| = 1.0 \times 10^7 \frac{\text{V}}{\text{m}}$, λ^{in} , ΔE^{in} (B3LYP/6-311G*), $T = 300 \text{ K}$. The Kondo parameter is $\alpha = 3.6$ in the Weiss-Dorsey rates.

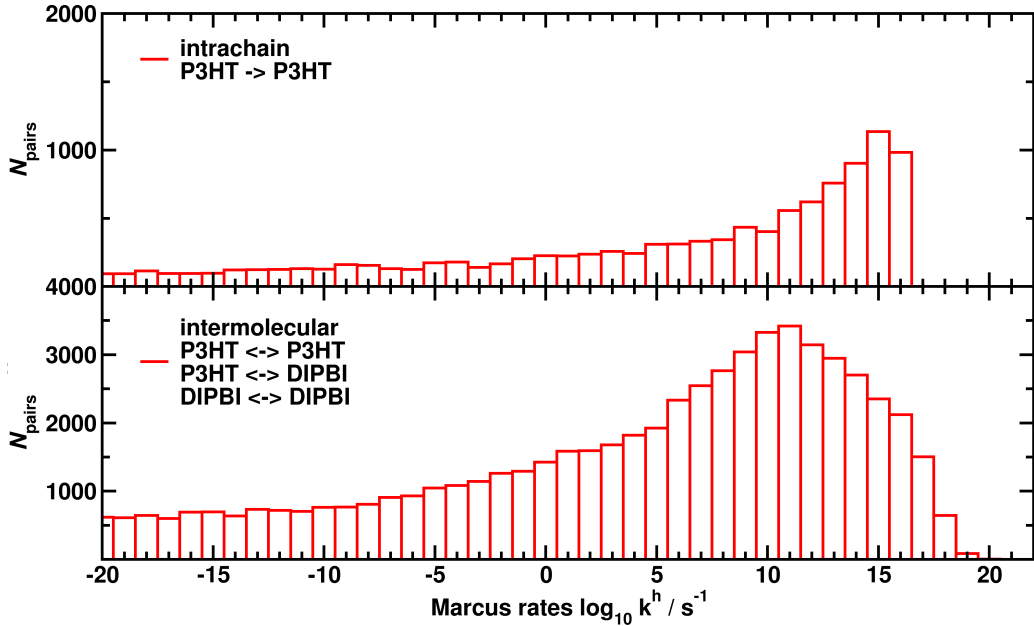


Figure 4.25: (a) Charge transfer rate distribution for intrachain $\text{P3HT} \leftrightarrow \text{P3HT}$ transitions in a P3HT:DIPBI morphology at 500 K with Marcus rates for hole transfer. (b) Distribution for intermolecular transitions $\text{P3HT} \leftrightarrow \text{P3HT}$, $\text{P3HT} \leftrightarrow \text{DIPBI}$, and $\text{DIPBI} \leftrightarrow \text{DIPBI}$. All rate types are evaluated using the following parametrisation including CDFT-based charge transfer integrals $|J_{AB}|$ in the ($n_A = 1 \& n_B = 1$) approximation (Fig. 3.21), $|\mathbf{F}_z^{\text{ext}}| = 1.0 \times 10^7 \text{ V m}^{-1}$, λ^{in} , ΔE^{in} (B3LYP/6-311G*), $T = 300 \text{ K}$.

The direct comparison of intrachain and intermolecular Marcus rates shows that some of the intermolecular rates are greater than the intrachain rates (Fig. 4.25). This is consistent with the higher number of simulated intermolecular hoppings found compared to intrachain hoppings. It should also be noted here that there is a significant proportion of 18% intrachain rates that favor the direction of longer segment lengths within the chain, whereas the reverse rate can be more than four orders of magnitude smaller.

The distributions of charge transfer rates are displayed in Figure 4.26 for hopping pairs located at the donor/acceptor interface. Holes transitions from DIPBI to P3HT yield higher values and narrower width of rate distributions for all three types of rate compared to those in the opposite direction P3HT \rightarrow DIPBI. In general, the physically preferred direction of hole transfer is correctly reproduced by all rate types. Visual comparison of the rate distributions suggests that the Weiss-Dorsey and Jortner rates are higher than the corresponding Marcus rates.

These findings are also reflected numerically in the averaged $\log_{10} k^h$ for DIPBI \rightarrow P3HT transitions. They yield $\log_{10} k^h = (7.15 \pm 8.10) \text{ s}^{-1}$ for Weiss-Dorsey rates, $(7.89 \pm 7.91) \text{ s}^{-1}$ for Jortner rates and $(5.76 \pm 7.90) \text{ s}^{-1}$ for Marcus rates. The P3HT \rightarrow DIPBI rates exhibit $\log_{10} k^h = (2.09 \pm 9.58) \text{ s}^{-1}$ for Weiss-Dorsey, higher values for Jortner rates $(6.14 \pm 9.13) \text{ s}^{-1}$ and a broad distribution for Marcus rates with $(0.65 \pm 10.61) \text{ s}^{-1}$. Therefore, all P3HT \rightarrow DIPBI hole transfer distributions are centred at lower values than those for DIPBI \rightarrow P3HT.

If we take a look at the rate distributions for electron transfer at the donor/acceptor interface in the P3HT:DIPBI morphology (Fig. 4.26), we see that Marcus electron transfer rates for P3HT/DIPBI transitions are very tiny.

Weiss-Dorsey rates exhibit small electron transfer rates $\overline{\log_{10} k^e} = (-0.36 \pm 5.15) \text{ s}^{-1}$. Moreover, only Jortner rates possess a moderate distribution $\overline{\log_{10} k^e} = (3.41 \pm 5.84) \text{ s}^{-1}$. Both distributions are shifted to lower transfer rates compared to hole transfer rates. The electron rates in the inverse direction from DIPBI to P3HT are all numerically zero. The Marcus rate distributions indicate that they lead to physically incorrect electron trajectories in kMC simulations, if they are applied to the P3HT:DIPBI morphology. Therefore, the computation of electron mobilities in P3HT:DIPBI based on Marcus rates is obsolete.

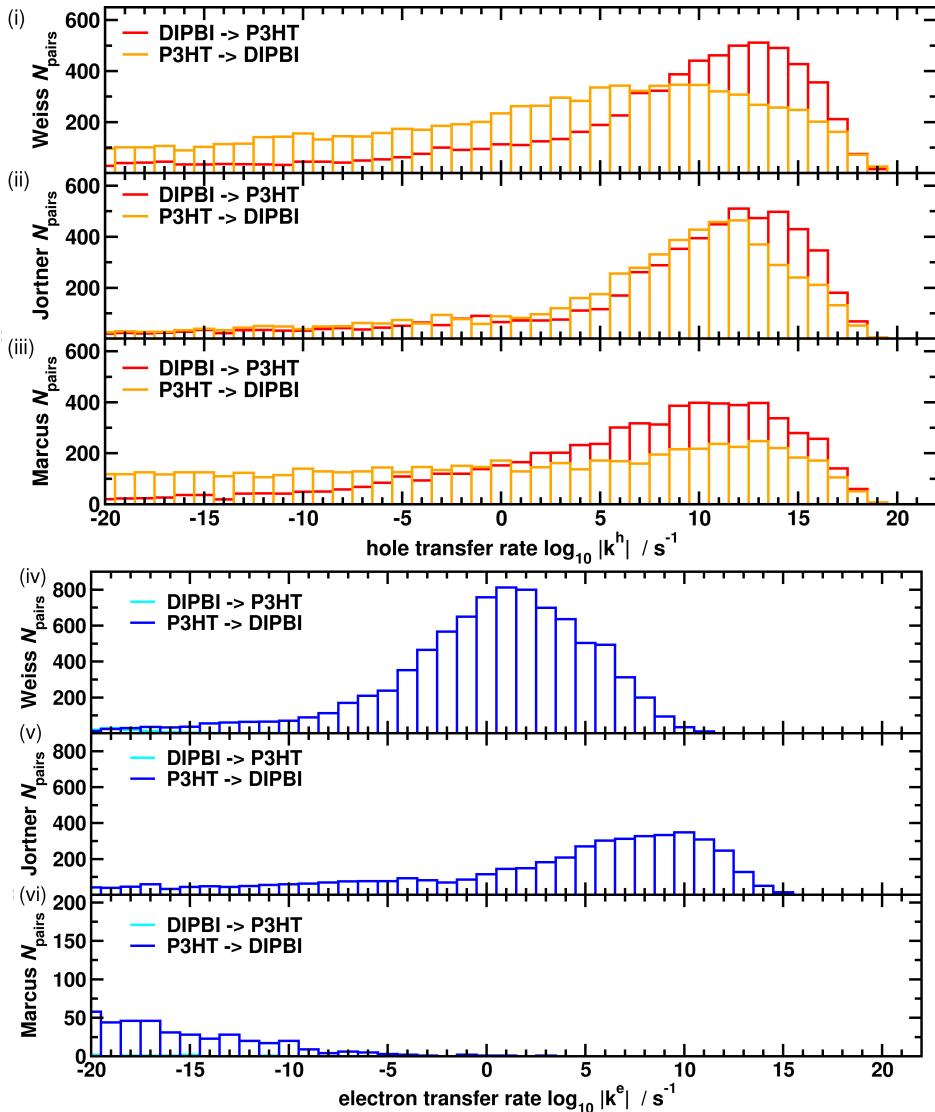


Figure 4.26: Charge transfer rate distributions at the interface for DIPBI→P3HT and P3HT→DIPBI transitions in a P3HT:DIPBI morphology at 500 K with Weiss-Dorsey rates (i,iv), Jortner rates (ii,v) and Marcus rates (iii,vi) for hole (red,orange) and electron transfer (blue). Electron rates in DIPBI→P3HT (cyan) transitions are numerically zero. The rates are evaluated for the following parametrisation with scaled PM3 $|J_{AB}|$ to CDFT, $|\mathbf{F}_z^{\text{ext}}| = 1.0 \times 10^7 \frac{\text{V}}{\text{m}}$, λ^{in} , ΔE^{in} (B3LYP/6-311G*), $T = 300 \text{ K}$.

4.1.3.8 Electron Transport

We perform kMC simulations for electron transport combining intermolecular and intramolecular charge transfer in the P3HT:DIPBI morphology at 500 K. The calculations are based on the rate distributions presented in section 4.1.3.7.

The electron mobilities in P3HT:DIPBI is $\mu_{\text{tot}}^e = (1.31 \pm 0.50) \text{ cm}^2/\text{Vs}$ for Weiss-Dorsey rates, which exceeds the value for Jortner rates $\mu_{\text{tot}}^e = (2.54 \pm 0.62) \times 10^{-1} \text{ cm}^2/\text{Vs}$. These values are surprisingly close to the experimental results for the electron mobility in pure, organic single-crystal DIPBI transistors, where the charge carrier mobility is measured in the range from $\mu = 1 \text{ cm}^2/\text{Vs}$ up to $\mu = 4.65 \text{ cm}^2/\text{Vs}$ [373]. Even though Marcus rates do not describe the electron dynamics at the donor/acceptor interface correctly (Fig. 4.26), we provide the electron mobility for Marcus rates $\mu_{\text{tot}}^e = (1.45 \pm 0.44) \times 10^{-2} \text{ cm}^2/\text{Vs}$ for comparison. We see that electron mobility in DIPBI exceeds the mobility in P3HT. This trend matches the experimental findings in P3HT:PCBM, where P3HT is the component limiting the charge carrier mobility [303, 367–369].

The kMC simulations with Jortner rates result in 59.8% DIPBI→DIPBI transitions, which is similar to those for Marcus rates 65.1%. In kMC simulations for electron transport based on Weiss-Dorsey rates, we see that the vast majority of transitions (99.8%) are DIPBI→DIPBI. Note, that P3HT→DIPBI and DIPBI→P3HT transitions between the different domains are rare events. So, Weiss-Dorsey rates guarantee that the electrons remain predominantly in the acceptor domain.

We determine the electron pathways with the lowest resistance that cross the simulation box in y -direction using Dijkstra algorithm (Fig. 4.27). They are based on kMC simulations for Jortner (Fig. 4.27,i) and Weiss-Dorsey electron transfer rates (Fig. 4.27,ii) employing intermolecular and intramolecular electron transport. Several low-resistance pathways connect the start and end zones for both rate types.

The application of the Jortner rates mainly results in low resistance pathways consisting of P3HT molecules. However, the pathway with the lowest resistance for Jortner rates contains 88 P3HT segments but also 18 DIPBI molecules. In the P3HT domain, we find that 61% of all transitions are intrachain and 39% are interchain.

If we turn to the electron pathways of low resistance for Weiss-Dorsey rates (Fig. 4.27,ii), we also find that several pathways contain thiophene chains with small resistance. Some sections coincide with the those found for Jortner rates. In contrast to Jortner rates, Weiss-Dorsey rates yield a high portion of DIPBI molecules in the pathways. The lowest resistance pathway for Weiss-Dorsey rates consists predominantly of DIPBI molecules and also involves sections with P3HT segments (Fig. 4.27,ii).

The pathway consists of 88 DIPBI molecules and 16 P3HT segments with a thiophene chain length between $n = 1$ and $n = 11$. The P3HT section contains seven intramolecular and nine intermolecular transitions between P3HT segments. It is linked to a long electron transport channel, which is made up of DIPBI molecules only. The continuous DIPBI channel exhibits different stacking motives with DIPBI/DIPBI pairs. Visual inspection details that the majority of all pairs (57%) show a face-on π -stacking motive. A share of 11% of all pairs exhibit π -stacking with a lateral shift between the DIPBI molecules. Moreover, we find a high portion of about 26% pairs where the pairs are aligned roughly orthogonal to each other, forming T -stacks. A smaller percentage of about 6% of pairs show lateral alignment. Hence, different aggregation alignments of DIPBI molecules contribute to the low resistance channel.

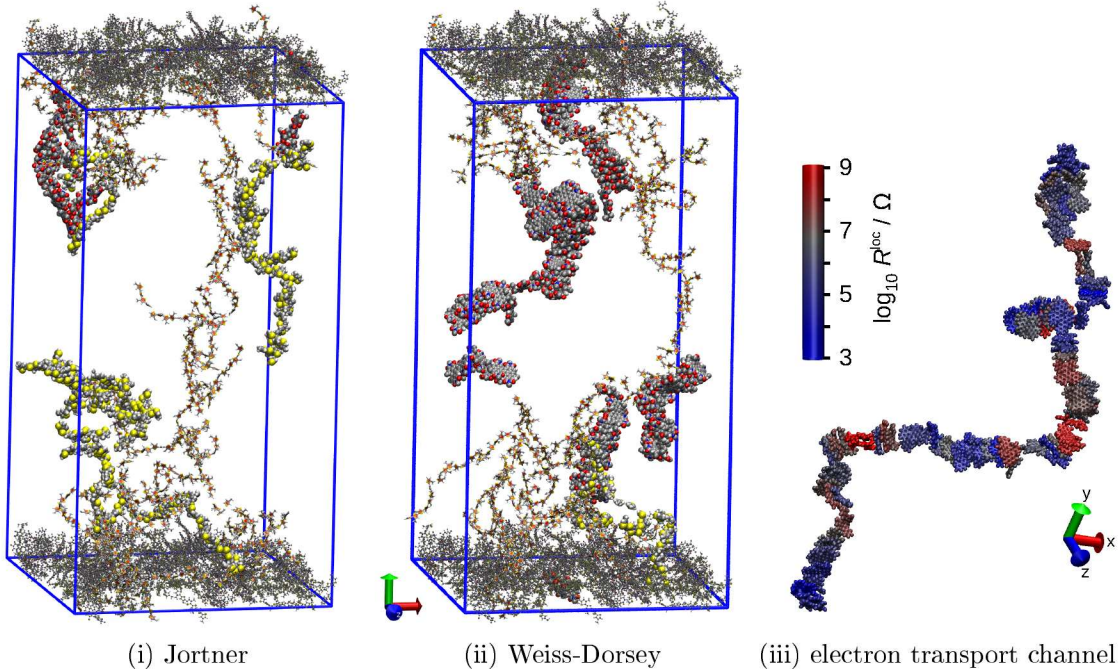


Figure 4.27: Electron transport pathways with small electronic resistance in P3HT:DIPBI morphology based on (i) Jortner and (ii) Weiss-Dorsey transfer rates using the Dijkstra algorithm. The pathways are determined for every molecule in the start zone (black, below) to those in the end zone (black, above). The molecules, which belong to the pathways are depicted in the paper chain representation (orange) and the one with lowest total resistance $|R^{\text{tot}}|$ is depicted in VdW representation. Note that the continuous pathways contain linked images using periodic boundary conditions. (iii) Electron transport channel of DIPBI molecules and colour-coded local resistance $\log_{10} R^{\text{loc}}$ based on Weiss-Dorsey rates.

We observe that the local resistance R^{loc} is correlated to the relative orientation of DIPBI pairs along the electron transport channel (Fig. 4.27,iii). We find the tendency that sections with dominating π -stacking character give rise to low R^{loc} (blue), whereas T -stacking or lateral alignments of DIPBI molecules can act as local barriers for electron transport with elevated R^{loc} (red). As T -stacks or lateral dimer arrangements introduce windings and curvatures in the electron transport channel, they play an essential role in the conductive connectivity between predominantly linear aligned sections of π -stacks.

These findings based on kMC simulations corroborate the results from optimised DIPBI dimer configurations in the electronic ground state (see Sec. 3.1.1). We see that the DIPBI dimers (Fig. 3.3) yield similar stacking motives as found in the electron transport channel in the amorphous blend morphology (Fig. 4.27,iii). Moreover, the favourable features for electron transfer (Tab. 3.1) in π -stacks are also reflected in the charge transport simulations. Even though some dimer configurations are high in total energy, i.e. they do not contribute if a Boltzmann averaging is applied, both approaches underline the importance of T -stacking or lateral dimer alignments. Thus, basic charge transfer properties for dimers can give relevant insight into charge transport characteristics in the amorphous phase. These findings are key motivating factors for the analysis of aggregation patterns and charge transfer properties based on dimers and study trends for different electron acceptor molecules (see Sec. 5).

4.1. MULTISCALE MODEL FOR CHARGE TRANSPORT IN P3HT AND P3HT:DIPBI143

Averaging the pathways of minimal resistance connecting all molecules in start zone to the end zone yields a higher resistance for Jortner rates $\bar{R} = 1.4 \times 10^{10} \Omega$ than for Weiss-Dorsey rates $\bar{R} = 5.6 \times 10^8 \Omega$. This is in line with the higher mobility for Weiss-Dorsey rates in comparison to Jortner rates.

In total, we find facilitated electron transport along extended charge transport channels of DIPBI using kMC simulations with Weiss-Dorsey rates. The multiscale model especially helps to identify molecular packing arrangements that are beneficial for electron transport.

4.1.3.9 Conclusion P3HT:DIPBI

A multiscale model to investigate the interplay of donor and acceptor components in a P3HT:DIPBI donor-acceptor blend and the resulting effects on charge transport properties in an bulk heterojunction organic solar cell has been presented. It employs morphologies obtained from coarse-grained molecular dynamics simulations, back-mapped onto an atomistic representation, and charge transport simulations using the kinetic Monte Carlo method in combination with Marcus, Jortner and Weiss-Dorsey charge transfer rates, which are parametrised using first principles or semiempirical electronic structure approaches. We find that the choice of method to compute charge transfer integrals and reorganization energies can influence the resulting charge carrier mobilities immensely. Linear scaling factors have been established to enable the use of DIPRO-based charge transfer integrals from computationally efficient semiempirical methods whilst maintaining the order of magnitude of CDFT reference data. Comparison of kMC simulations with and without intramolecular charge transfer within the P3HT oligomers clearly reveal the importance of intramolecular contributions to the overall charge carrier mobility. The analysis of low resistance pathways established useful correlations between hole transport efficiency and local morphology. In particular, we find predominant hole transport along extended P3HT chains and electron transport along channels of aggregated DIPBI molecules consisting of combinations of different stacking arrangements. The model can help to understand the interplay of intramolecular and intermolecular charge transfer in amorphous materials.

4.2 Multiscale Model for Charge Transport in PPDI and PBDT-TS1:PPDI

The PBDT-TS1:PPDI organic solar cell [311] consists of the donor polymer PBDT-TS1 [390] and the non-fullerene small acceptor molecule PPDI (Fig. 4.28). The two-dimensional conjugated polymer PBDT-TS1 contains the benzo[1,2-b:4,5-b']dithiophene (BDT) unit [391] in combination with the thieno[3,4-b]thiophen motive [392]. PPDI is a non-planar dimeric PDI derivative [393]. In a PBDT-TS1:PPDI device one can obtain a PCE of about 5.40% [311], which exceeds the PCE in P3HT:DIPBI. For PBDT-TS1:PC₇₁BM, an even higher value of 9.48% can be obtained [390]. The BDT unit is also present in the A-D-A copolymer donor D18, which achieves an outstanding high PCE of 18.2% [16] in combination with Y6 [394].

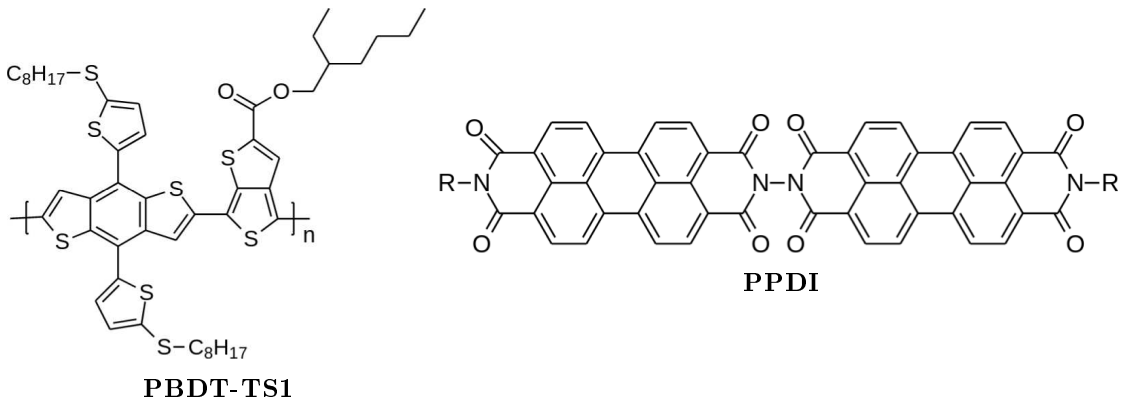


Figure 4.28: Chemical structures of the donor PBDT-TS1 and acceptor PPDI [311].

The goal of this chapter is to simulate and analyse charge transport in the PBDT-TS1:PPDI blend using a refined multiscale modelling approach compared to DIPBI:P3HT. Therefore, we first focus on the acceptor molecule PPDI, discuss aggregation patterns and basic charge transfer properties. Based on these considerations, we simulate charge transport in amorphous PPDI (Sec. 4.2.2) and study the impact of outer-sphere contributions and the site-energy difference on the charge carrier mobilities. In a subsequent step, we analyse the electronic structure of the donor polymer PBDT-TS1 (Sec. 4.2.3), which gives rise to a partitioning schema to simulate intramolecular charge transport (Sec. 4.2.4). Moreover, kMC simulations require internal reorganization energies and site-energy differences (Sec. 4.2.5). Finally, all these considerations allow the modelling of hole and electron transport in amorphous PBDT-TS1:PPDI (Sec. 4.2.6). The computational details are summarised in section 2.2.4.

4.2.1 Acceptor Molecule PPDI

The PPDI molecule consists of two PDI units connected by an N-N bond. The PDI arms are roughly orthogonal to each other, and each unit possesses a branched residual group $R=CH-(C_5H_{11})_2$. The frontier orbitals in PPDI are delocalised over both PDI subunits, therefore the PPDI is considered as a single hopping site in kMC simulations (Fig. 4.29). The extension of the conjugated π -system is about 27.5 Å along the main molecular axis. Furthermore, the aliphatic side chains have no influence on the localisation of the frontier orbitals and are substituted by isopropyl rest groups in the $|J_{AB}|$ DIPRO calculations.

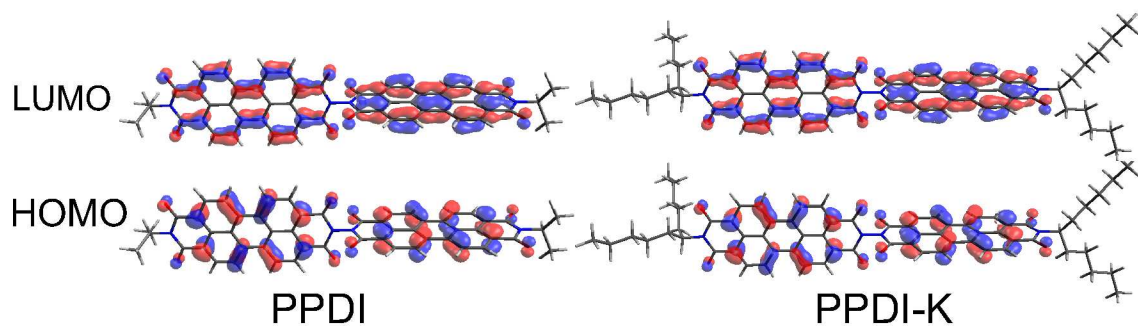


Figure 4.29: PPDI frontier orbitals HOMO and LUMO at the optimised ground state energy S_0 (B3LYP/6-311G**). The frontier orbitals are delocalised over both PBI subunits, therefore the PPDI molecule is regarded as a single hopping site. The aliphatic side chains have no impact on the localisation of the frontier orbitals.

The pairs of the frontier orbital energy levels are energetically degenerate in PPDI, e.g. HOMO/HOMO-1 and LUMO/LUMO+1. Therefore, additional consideration is required when determining the charge transfer integral in conjugation with the DIPRO approach.

$$|J_{AB}| = \sqrt{\sum_{i,j} \frac{|\langle \phi_i | H | \phi_j \rangle|^2}{4}} \quad \text{for } i, j \in \begin{cases} \text{HOMO, HOMO-1} & \text{for hole transfer} \\ \text{LUMO, LUMO+1} & \text{for electron transfer} \end{cases} \quad (285)$$

This approximation is applied, if the Kohn-Sham frontier orbital energy difference is $\Delta\epsilon_{ij} < k_B T \approx 0.025$ eV.

The study of different aggregation patterns for PPDI dimers yields five distinct local minimum structures in the ground state S_0 . They are labelled as PPDI (*A* - *E*) and ordered according to their relative total ground state energy (Fig. 4.30).

The PPDI dimers *A*, *B* and *C* show π -stacking of one PDI blade, whereas the other blades are aligned roughly orthogonal to the stacking direction. The interacting blades are always slightly inclined towards each other. We define an internal bending angle ϕ for a PPDI molecule as the enclosed angle of both terminal nitrogens and the geometric centre between two nitrogen atoms in the middle of a PPDI molecule. The straight orientation of the monomers in configurations *A* to *C* is represented by large bending angles, which are in the range of $\phi \approx 167 - 177^\circ$. As the PPDIIs are nearly linear in configurations *A* to *C*, we can evaluate the relative rotatory angle θ between both PPDI molecules as the enclosed angle between the straight lines connecting both terminal nitrogen atoms. In this way, configurations *A* to *C* exhibit $\theta = 74^\circ$, $\theta = 40^\circ$, and $\theta = 46^\circ$, respectively.

In contrast, both blades are aligned in a stacking fashion in dimer PPDI configurations *D* and *E*. They are higher in energy E_{rel} than the dimer configurations *A* to *C*. The parallel, shifted alignment in configuration *D* is represented by a small angle $\theta = 12^\circ$. Both monomers are more interleaved in the PPDI configuration *E*, and hence both monomers exhibit internal bending angle about $\phi = 153^\circ$ and $\phi = 158^\circ$, respectively.

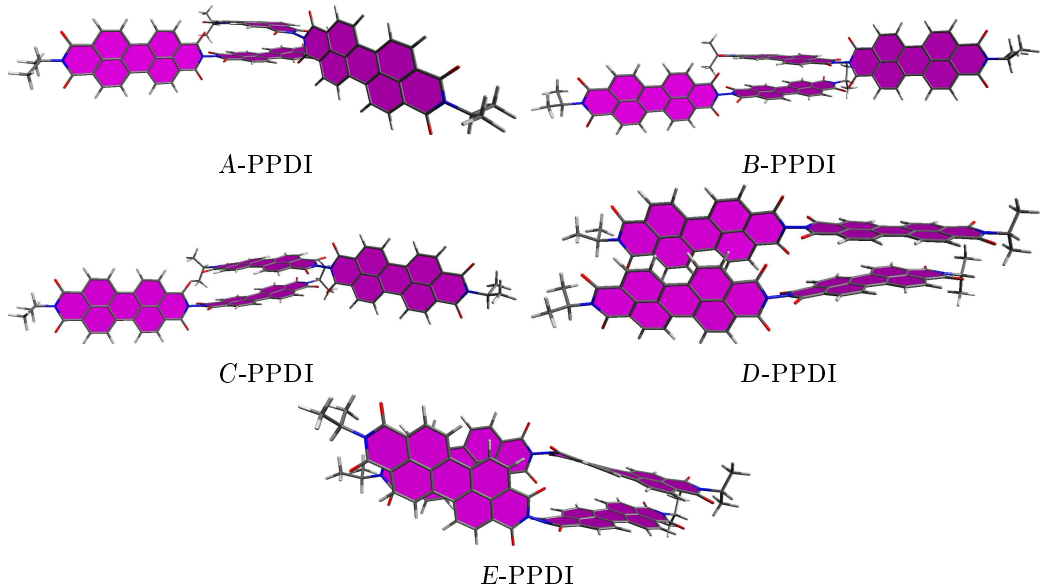


Figure 4.30: Optimised ground state geometries of stacking aggregates for PPDI dimers on B3LYP-D3(BJ)/6-31G* level of theory. The different dimer structures are labelled with *A* to *E*. The PDI aromatic rings are marked in violet.

On average, PPDI dimers yield $|\bar{J}_{AB}^h| = (4.34 \pm 4.12) \times 10^{-2}$ eV for the hole charge transfer integral and a slightly lower value of $|\bar{J}_{AB}^e| = (2.63 \pm 2.55) \times 10^{-2}$ eV for electron transfer (Tab. 4.1). Especially, configuration *A*-PPDI yields a high value for the hole transfer integral and therefore also an elevated Marcus rate.

As the dimer configurations *D* and *E* possess two interacting PBI blades, they exhibit higher rates than conformations *A* to *C*. Moreover, the resulting Marcus charge transfer rates for electrons $\bar{k}_{AB}^e = (2.83 \pm 3.41) \times 10^{13}$ s⁻¹ are slightly higher than those for holes $\bar{k}_{AB}^h = (2.02 \pm 2.94) \times 10^{13}$ s⁻¹.

Table 4.1: Marcus charge transfer rates between optimised dimer structures for PPDI for hole transfer k_{AB}^h and for electron transfer k_{AB}^e on B3LYP-D3(BJ)/6-31G* level of theory. Furthermore, the relative energies are presented concerning the most stable aggregation and the charge transfer integral $|J_{AB}|$ from the DIPRO calculations

dimer conformation	$E_{\text{rel}} / \text{eV}$	$ J_{AB}^h / \text{eV}$	k_{AB}^h / s^{-1}	$ J_{AB}^e / \text{eV}$	k_{AB}^e / s^{-1}
<i>A</i> -PPDI	0.000	1.06E-1	2.55E+13	8.96E-3	3.24E+12
<i>B</i> -PPDI	0.184	5.83E-3	1.75E+10	3.31E-3	5.07E+11
<i>C</i> -PPDI	0.292	1.76E-2	1.12E+11	1.17E-2	6.39E+12
<i>D</i> -PPDI	0.797	2.41E-2	6.11E+12	4.97E-2	6.44E+13
<i>E</i> -PPDI	0.912	6.31E-2	6.94E+13	5.80E-2	6.70E+13

4.2.2 kMC Simulations in Amorphous PPDI

We perform kMC simulations in an amorphous PPDI morphology containing 800 molecules, and we evaluate the charge carrier mobilities. Especially, we focus on the influence of different modelling approaches on the mobilities, e.g. using the Thole model with and without induction effects for λ^{out} (Eq. 228) and E^{out} (Eq. 235,241,242).

Morphology and Charge Transport Simulations The atomistic morphology (Fig. 4.31,i) shows the PPDI molecules in an amorphous phase with a disordered packing. This morphology is applied in the subsequent kMC simulations, where we assign a hopping site (Fig. 4.31,ii) to every molecule. The centres for each site are located at the COM (without the side chains). We observe clusters of these hopping sites, which correspond to π -stacking PPDI molecules. If we perform kMC simulations for electron transport (see Comp. Details 2.2.3), we obtain the occupation numbers p_e^{occ} and can determine the sites with the highest 10% occupations (Fig. 4.31,iii). We can see six molecules with $p_e^{\text{occ}} > 10^{-2}$, where the charge stays a long time. The charge carrier pathway with the lowest resistance (Eq. 284) involves π -stacking and lateral arrangements of PDI units between pairs (Fig. 4.31,iv).

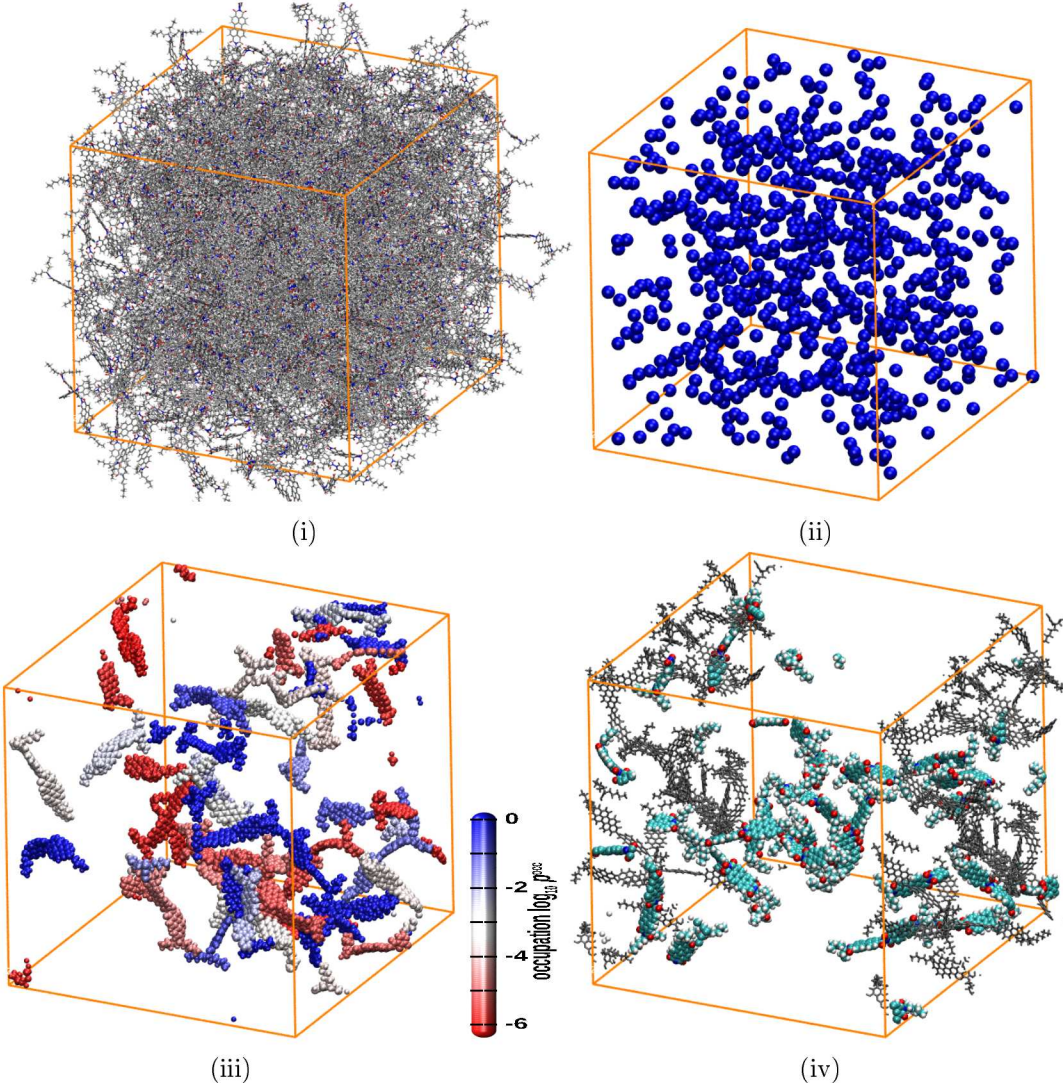


Figure 4.31: (i) Atomistic morphology with 800 PPDI molecules in the simulation box (orange). (ii) Hopping sites inside the morphology (blue dots). (iii) Molecules with the 10% highest occupation numbers for electrons transport in kMC simulations. (iv) Pathway with the lowest resistance for electron transport. Black molecules mark the start and zone for the Dijkstra algorithm.

Charge Carrier Mobilities The initial setup for kMC simulations on PPDI yields a charge carrier mobility $\mu_{\text{tot}}^{\text{h}} = (3.91 \pm 5.56) \times 10^{-11} \text{ cm}^2/\text{Vs}$ and an electron mobility $\mu_{\text{tot}}^{\text{e}} = (2.92 \pm 1.43) \times 10^{-12} \text{ cm}^2/\text{Vs}$. The initial distributions for $|J_{AB}|$ (Fig. A.22), the Marcus rates (Fig. A.25) and site energies E_i and λ^{out} (Fig. A.23) are found elsewhere.

The reported experimental results for the electron mobility in a pristine film state a maximum $\mu_{\text{exp}}^{\text{e}} = 4.1 \times 10^{-4} \text{ cm}^2/\text{Vs}$ for PPDI [311]. Indeed, one cannot expect completely similar results for the pristine film and the amorphous MM-morphology. As deviations are large, we modify the setup for the Marcus rates.

As a first approach, we employ a scaling of the ZINDO/MOO-based charge transfer integral to CDFT. It leads to a higher hole mobility, but still poor results $\mu_{\text{tot}}^{\text{h}} = (2.71 \pm 2.02) \times 10^{-10} \text{ cm}^2/\text{Vs}$. The electron mobility is even lower $\mu_{\text{tot}}^{\text{e}} = (7.25 \pm 3.11) \times 10^{-13} \text{ cm}^2/\text{Vs}$.

We turn the scaling off again and study the impact of E^{out} and λ^{out} on μ_{tot} . If only electrostatic contributions (excluding induction effects) are included in E^{out} , but λ^{out} is set to zero, we observe an increase in mobility $\mu_{\text{tot}}^{\text{e}} = (6.73 \pm 56.4) \times 10^{-9} \text{ cm}^2/\text{Vs}$ and $\mu_{\text{tot}}^{\text{h}} = (4.20 \pm 2.00) \times 10^{-11} \text{ cm}^2/\text{Vs}$. We can get even closer to the experimental data if λ^{out} is included and E^{out} is set to zero. So, we obtain $\mu_{\text{tot}}^{\text{e}} = (6.13 \pm 2.80) \times 10^{-5} \text{ cm}^2/\text{Vs}$ and $\mu_{\text{tot}}^{\text{h}} = (1.08 \pm 1.66) \times 10^{-5} \text{ cm}^2/\text{Vs}$. If λ^{out} is applied and scaled charge transfer integrals from ZINDO/MOO to CDFT are applied, then the charge carrier mobilities increase further to $\mu_{\text{tot}}^{\text{e}} = (7.83 \pm 4.62) \times 10^{-5} \text{ cm}^2/\text{Vs}$ and $\mu_{\text{tot}}^{\text{h}} = (1.33 \pm 1.26) \times 10^{-5} \text{ cm}^2/\text{Vs}$, respectively.

In the case, if all outer-sphere contributions are neglected ($\lambda^{\text{out}} = 0.0 \text{ eV}$ and $E^{\text{out}} = 0.0 \text{ eV}$), the mobilities overestimate the experimental data. The electron mobility is slightly higher $\mu_{\text{tot}}^{\text{e}} = (2.96 \pm 0.03) \times 10^{-2} \text{ cm}^2/\text{Vs}$ than the hole mobility $\mu_{\text{tot}}^{\text{h}} = (1.08 \pm 0.04) \times 10^{-2} \text{ cm}^2/\text{Vs}$.

If we employ the induction effects for the site energies using the Thole model in line with CHelpG partial charges on the atomic centres with unscaled Thole polarisabilities, λ^{out} and scaled ZINDO/MOO to CDFT charge transfer integrals for the PPDI morphology, then one obtains an electron mobility $\mu_{\text{tot}}^{\text{e}} = (1.23 \pm 0.25) \times 10^{-8} \text{ cm}^2/\text{Vs}$. For holes, one obtains $\mu_{\text{tot}}^{\text{h}} = (5.67 \pm 2.92) \times 10^{-9} \text{ cm}^2/\text{Vs}$.

In a subsequent step, we scale the initial polarisabilities (see Sec. 1.4.4.4) from the Thole model in such a way that they reproduce the effective molecular polarisable volume, which is $V_{\text{pol}} \approx 131.3 \text{ \AA}^3$ in QM calculations (B3LYP-D3(BJ)/6-31G*) for a neutral PPDI molecule. In this fashion, one obtains the scaled atomic polarisabilities $\alpha_{\text{H}} = 0.608 \text{ \AA}^3$, $\alpha_{\text{N}} = 1.316 \text{ \AA}^3$, $\alpha_{\text{O}} = 1.026 \text{ \AA}^3$, $\alpha_{\text{C}} = 1.636 \text{ \AA}^3$ for each atom type in the PPDI molecule. Using these scaled Thole polarisabilities, one obtains $\mu_{\text{tot}}^{\text{h}} = (2.33 \pm 0.51) \times 10^{-6} \text{ cm}^2/\text{Vs}$ and for electrons $\mu_{\text{tot}}^{\text{e}} = (1.96 \pm 0.32) \times 10^{-7} \text{ cm}^2/\text{Vs}$, if the induction effects are included. In turn, if the induction effects are not present, one obtains a hole mobility $\mu_{\text{tot}}^{\text{h}} = (2.90 \pm 0.37) \times 10^{-6} \text{ cm}^2/\text{Vs}$ and $\mu_{\text{tot}}^{\text{e}} = (8.96 \pm 1.15) \times 10^{-8} \text{ cm}^2/\text{Vs}$.

An alternative approach is the GDMA approach (Eq. 240) using distributed multipoles to determine $\Delta E_{\text{AB}}^{\text{el}}$ and $\Delta E_{\text{AB}}^{\text{pol}}$ in the Thole framework. However, multipole expansion to quadrupole moments were tested and resulted in unphysically high energies $E_{\text{AB}}^{\text{el}}$ and $E_{\text{AB}}^{\text{pol}}$. Consequently, they are not presented here.

In general, we see that the evaluated hole and electron mobilities are not at the same order of magnitude as the experimental data, and even though different models are employed to determine the outer-sphere contribution, these methods do not lead to a significant improvement in the approximation to the experimental results. However, the investigation details different approaches to modelling mobilities by using kMC simulations.

Distribution of Site Energy Differences We focus on the distributions of the site-energy difference ΔE_{AB} (Fig. 4.32) in order to gain some insight into the vast deviations in the charge carrier mobilities from kMC simulations (see Sec. 4.2.2). As only PPDI molecules are present in the amorphous morphology, the internal site-energy difference ΔE_{AB}^{in} is always zero (Eq. 200). If just the contribution to the site-energy difference ΔE_{AB}^{ext} due to an external field in $F_z^{ext} = 1.0 \times 10^7 \text{ V m}^{-1}$ is determined (Eq. 201), one obtains a distribution for holes, which is centred roughly around the origin at $-9.01 \times 10^{-4} \text{ eV}$ and has a standard deviation of about $\sigma^{ext} = 1.3 \times 10^{-2} \text{ eV}$. The ΔE_{AB}^{ext} values switch their sign for electrons. The inclusion of electrostatic effects ΔE_{AB}^{el} due to outer-sphere contributions (Eq. 235) from the Thole model yields broad distributions for holes $\Delta E_{AB}^{ext} + \Delta E_{AB}^{el} = (-0.009 \pm 0.898) \text{ eV}$ and electrons $(-0.051 \pm 0.767) \text{ eV}$. If polarisation effects ΔE_{AB}^{pol} (Eq. 241) are included, the total site-energy differences are $\Delta E_{AB}^h = (0.004 \pm 0.188) \text{ eV}$ and $\Delta E_{AB}^e = (0.025 \pm 0.254) \text{ eV}$, so the width in the distributions is decreased.

A scaling of the atomic Thole polarisabilities to match the molecular polarisable volume yields $\Delta E_{AB}^{ext} + \Delta E_{AB}^{el*} = (-0.016 \pm 0.251) \text{ eV}$ for holes and similar values for electrons $(0.017 \pm 0.245) \text{ eV}$. The distribution is narrower than in the unscaled case. The inclusion of polarisation effects E_{AB}^{pol*} with scaled polarisabilities yields $(0.0064 \pm 0.191) \text{ eV}$ for holes and $(0.026 \pm 0.256) \text{ eV}$ for electrons, which are slightly broader than in the unscaled case with E_{AB}^{pol} .

In total, we see that the choice of the method to determine ΔE_{AB} has an enormous impact on the order of magnitude in the charge carrier mobility from kMC simulations. Unfortunately, a more refined schema for ΔE_{AB} does not consequently yield better agreement with experimental mobilities.

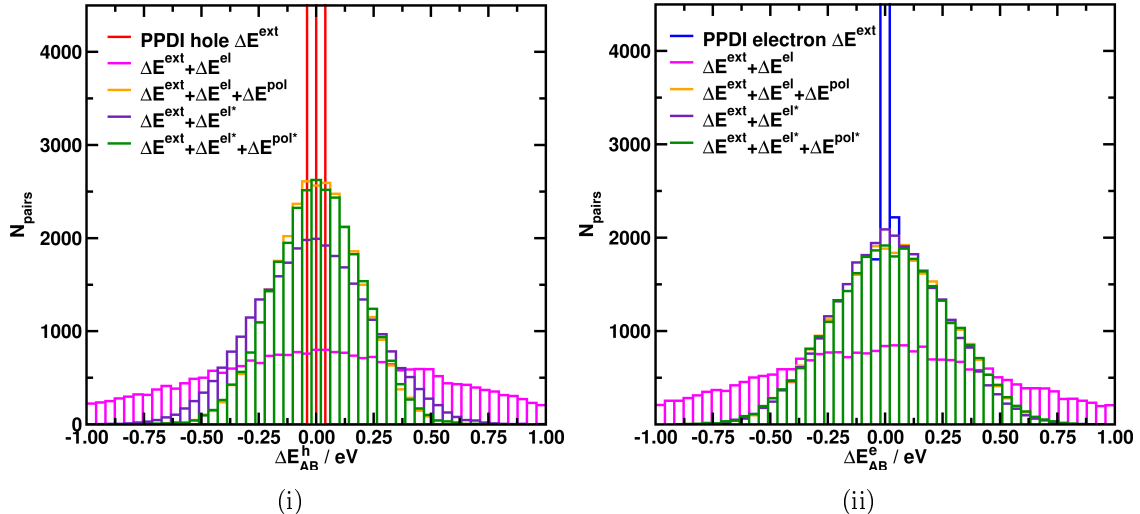


Figure 4.32: Distribution of site-energy difference ΔE_{AB}^h for (i) hole and (ii) electron transfer pairs ΔE_{AB}^e in PPDI morphology. The external field contribution ΔE_{AB}^{ext} is evaluated for an applied external electric field $F_z^{ext} = 1.0 \times 10^7 \text{ V m}^{-1}$. The Thole model is employed to evaluate electrostatic ΔE_{AB}^{el} and polarisation effects ΔE_{AB}^{pol} using a standard set of atomistic polarisabilities or scaled polarisabilities to match the molecular polarisable volume ΔE_{AB}^{el*} ΔE_{AB}^{pol*} . Partial charges are applied using the CHelpG method on B3LYP/6-311G** level of theory.

4.2.3 Electronic Structure of PBDT-TS1

The donor polymer PBDT-TS1 consists of n repetitive monomer units, which is made up of two subunits, the thienothiophene-based subunit (**A**) and the PBDT subunit (**B**) (Fig. 2.3). The labels (**A**) and (**B**) are introduced to facilitate the polymer sequence assignment, e.g. as $\mathbf{A}_n\mathbf{B}_n$, $\mathbf{A}_n\mathbf{B}_{n-1}$, and $\mathbf{A}_{n-1}\mathbf{B}_n$. We model the polymer chain to a maximum of $n = 8$ monomer units ($\mathbf{A}_8\mathbf{B}_8$).

First, we take a look at the electronic structure of the planar, linear polymer as a function of the chain length n (Fig. 4.33). Both HOMO and LUMO extend over the entire subunits **A** and **B**. In contrast, the frontier orbitals (B3LYP/6-31G*) only exhibit relevant contributions along the planar polymer backbone for $n \in [1, 8]$. Even though we increase the chain length, the frontier orbitals HOMO and LUMO remain delocalised only to a maximum of three to four monomer units (**AB**) along the PBDT-TS1 polymer chain. So, the frontier orbitals do not extend along the entire chain. In contrast to PPDI, the Kohn-Sham frontier orbital energies are not degenerated in PBDT-TS1 (Fig. A.26). Second, we extract a PBDT-TS1 chain from the amorphous, atomistic PBDT-TS1:PPDI morphology (Fig. A.27,ii). The chain contains several kinks and twists. As a consequence, the orbitals are confined on one or two subunits **A** and **B**.

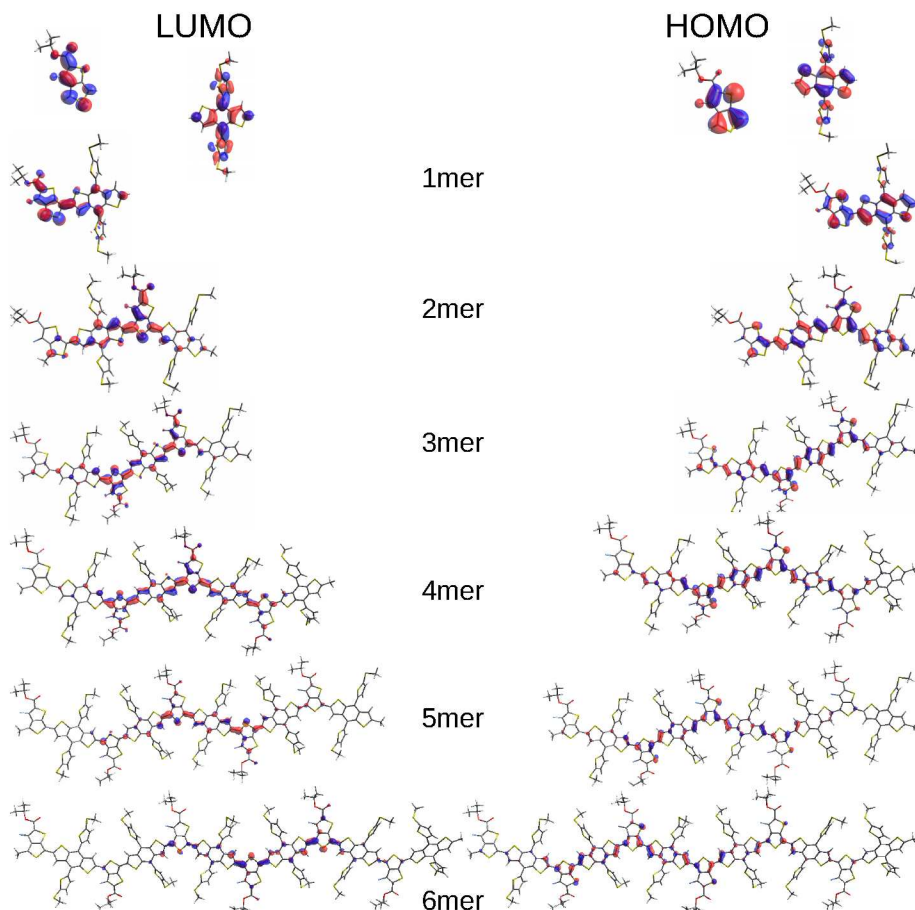


Figure 4.33: Frontier orbitals HOMO and LUMO for PBDT-TS1 polymer at the optimised neutral S_0 ground state geometry (B3LYP/6-31G*). The polymer is divided into subunits (1mer to 6mer) that consist of the building blocks thienothiophene-based unit (**A**) and PBDT (**B**). The excess charge is delocalised over three to four PBDT-TS1 subunits.

In analogy to the P3HT polymer, we want to describe the dynamic motion of the excess charge along the conjugated π -system in the PBDT-TS1 polymer backbone. Therefore, we introduce two dihedral angles $\theta(\mathbf{AB})$ and $\theta(\mathbf{BA})$ connecting two subunits in the order **AB** and **BA** (see Fig. 2.3). If we apply constrained geometry optimisations with a fixed dihedral angle $\theta(\mathbf{AB})$ to a single segment and alter θ in steps of $\theta(\mathbf{AB})=[40^\circ, 50^\circ, 60^\circ, 70^\circ, 80^\circ, 90^\circ]$ (Fig. A.27), we see that HOMO and LUMO are spread over both subunits **A** and **B** for 40° and 50° . For all $\theta \geq 60^\circ$ the orbitals are located only on a single subunit, e.g. the HOMO is located at **A** and the LUMO at **B**, respectively. Hence, we regard the SCCS dihedral angles $\theta_{\text{SCCS}}^{\text{cut}}(\mathbf{AB})$ and $\theta_{\text{SCCS}}^{\text{cut}}(\mathbf{BA}) = 60^\circ$ as a suitable cutoff criterion. We apply this partitioning schema of the PBDT-TS1 chain into segments to both angles $\theta(\mathbf{AB})$ and $\theta(\mathbf{BA})$ in order to reflect the limited orbital localisation of HOMO and LUMO (see Fig. 2.4).

4.2.4 Intramolecular Charge Transfer in PBDT-TS1 Polymer Chains

The intramolecular charge transport is determined for the polymer PBDT-TS1 using the CDFT/PBE/80Ry approach. Therefore, the intramolecular charge transfer integral $|J_{\text{DA}}^{\text{int}}|$ is evaluated *a priori* to kMC simulations as a function of the SCCS-dihedral angles $\theta(\mathbf{AB})$ and $\theta(\mathbf{BA})$ and interpolated by spline fits. As mentioned above, **(AB)** and **(BA)** label the order of the subunits. This treatment allows the decomposition of the polymer chain into conjugated segments, which are predominantly limited due to the kinks at the **AB** and **BA** linking junctions. This way, the influence of the relative orientation and alignment of the polymer segments on intramolecular transport inside the atomistic morphology is taken into account.

At the beginning, we perform constrained geometry optimisations on PBE/6-31G* level of theory, where the dihedral angle $\theta(\mathbf{AB})$ and accordingly $\theta(\mathbf{BA})$ is fixed, and all other nuclear degrees of freedom are allowed to relax. In this way, we obtain nuclear configurations with $\theta(\mathbf{AB})$ and $\theta(\mathbf{BA})$ in the range -180° to 180° in steps of $\Delta\theta = 10^\circ$. In a subsequent step, CDFT calculations are carried out to determine the intramolecular charge transfer integrals $|J_{\text{DA}}^{\text{int}}|$ and the vertical energy gap $\Delta E_{\text{DA}}^{\text{int}}$.

Figure 4.34 depicts SOMOs based on CDFT calculations for optimised geometries in **AB** (left) and **BA** (right) sequence at the cutoff dihedral angle $\theta_{\text{SCCS}}^{\text{cut}} = 60^\circ$. The excess charge is constrained to one of the polymer subunits **A** or **B** at a time. If we look at the hole transfer for unit **B** (**A/B⁺**, **B⁺/A**), the SOMO has contributions exclusively on **B**, whereas in the case of localisation on **A** (**A⁺/B**, **B/A⁺**), smaller contributions on subunit **B** can also be seen. In the case of electron transfer, the tendency is reversed. Here, the stronger localisation of the SOMO is found on **A** (**A⁻/B**, **B/A⁻**), while in the case of localisation on **B** (**A/B⁻**, **B⁻**/A), we note that considerable proportions of the SOMO also extend over subunit **A**. The latter feature is found more pronounced in **BA**, which is an indication of stronger intrachain electronic coupling during electron transfer compared to **AB**. The shape of the SOMOs for holes hardly differs for **AB** and **BA**, so that similar electronic couplings are expected.

The charge transfer integrals exhibit an M-shaped form as a function of θ with high values for planar configuration around 0° and $\pm 180^\circ$ (Fig. 4.35). The $|J_{\text{DA}}^{\text{h}}(\theta(\mathbf{AB}))|$ for hole transfer yields values from 0.05 eV to 0.53 eV in the range $\theta(\mathbf{AB}) = -180^\circ$ to -90° and reaches 0.69 eV in the 0° configuration. In the interval $\theta = [90^\circ, 180^\circ]$, the data is similar to the corresponding data in the range $\theta = [-180^\circ, -90^\circ]$. On average, $|J_{\text{DA}}^{\text{h}}(\theta(\mathbf{BA}))|$ yields higher values than $\theta(\mathbf{AB})$ from 0.08 eV to 0.64 eV in the range of $\theta(\mathbf{BA}) = -180^\circ$ to -90° but the maximum value 0.67 eV is slightly lower than the corresponding data for $\theta(\mathbf{AB})$ at $\theta = 0^\circ$.

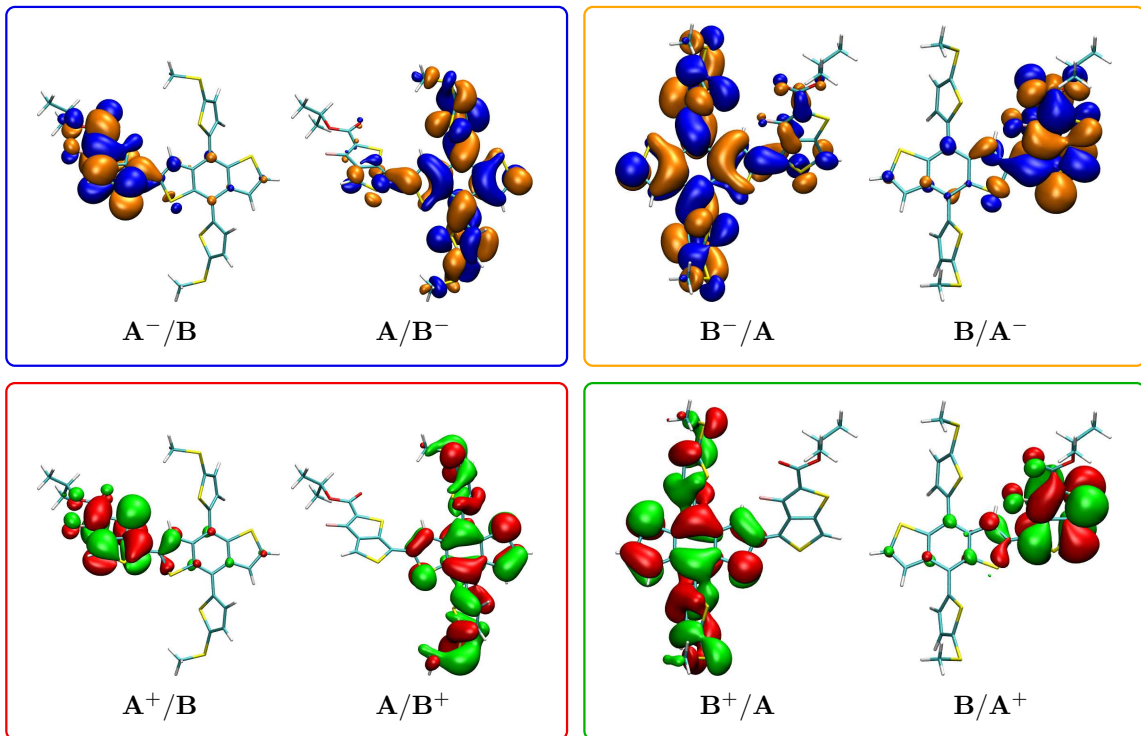


Figure 4.34: SOMOs with CDFT constraint for intrachain electron (top) and hole (bottom) transfer in PBDT-TS1. The excess charge is constrained to one of the polymer subunits **A** or **B** at a time. The polymer building blocks are arranged in the order **AB** (left) and **BA** (right). The geometries are optimised with a fixed dihedral angle $\theta_{\text{SCCS}}^{\text{cut}} = 60^\circ$ in the electronic ground state S_0 . We introduce a color-coding for electron transfer in **AB** (blue), **BA** (orange) and hole transfer in **AB** (red) and **BA** (green) (see Figs. 4.36 to 4.38).

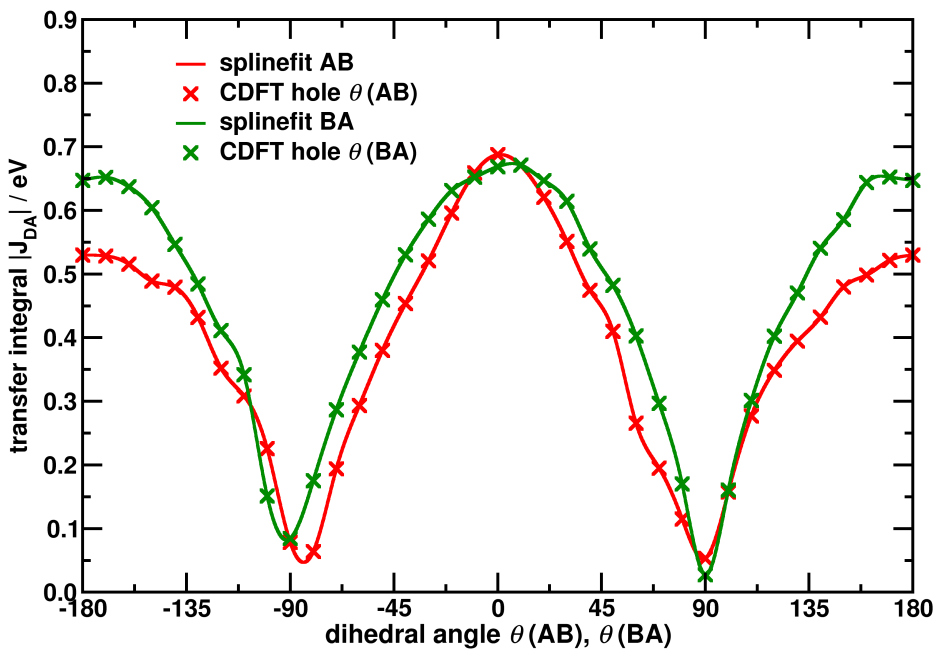


Figure 4.35: Transition matrix elements $|J_{\text{DA}}^h(\theta(\text{AB}))|$ and $|J_{\text{DA}}^h(\theta(\text{BA}))|$ for intramolecular hole transport (CDFT/PBE/80Ry) as a function of the SCCS dihedral angle $\theta(\text{AB})$ and $\theta(\text{BA})$ between two PBDT-TS1 segments in **AB** and **BA** sequence. Spline fits interpolate the data.

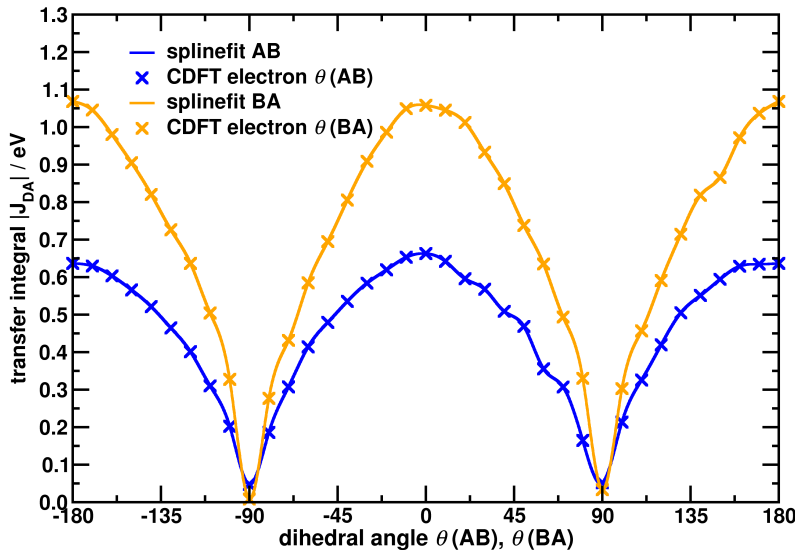


Figure 4.36: Transition matrix elements $|J_{DA}^e(\theta(\mathbf{AB}))|$ and $|J_{DA}^e(\theta(\mathbf{BA}))|$ for intramolecular electron transport on CDFT/PBE/80Ry level as a function of the dihedral angles $\theta(\mathbf{AB})$ and $\theta(\mathbf{BA})$ between two PBDT-TS1 segments in **AB** and **BA** sequence.

The maxima for the electron transfer integrals yield roughly similar magnitudes around $\theta = -180^\circ$ and 0° (Fig. 4.36). Especially, $|J_{DA}^e(\theta(\mathbf{BA}))|$ in **BA** configuration is enhanced (nearly doubled) to $|J_{DA}^e(\theta(\mathbf{AB}))|$, as the charge transfer integral yields values from 0.05 eV to 0.66 eV for $\theta(\mathbf{AB})$ compared to 0.01 eV to 1.07 eV for $\theta(\mathbf{BA})$.

In general, hole and electron transfer integrals in **AB** are always favoured over **BA** sequence $|J_{DA}^{h/e}(\theta(\mathbf{AB}))| > |J_{DA}^{h/e}(\theta(\mathbf{BA}))|$. The charge transfer integral for hole transport $|J_{DA}^h(\theta(\mathbf{AB}))|$ is always higher than those for electron transport as depicted in (Fig. 4.35) and (Fig. 4.36). The charge transfer integrals are lowest in the orthogonal orientations at about -90° and 90° , but the charge transfer integrals do not vanish, so even these extreme conformational cases do not entirely suppress intramolecular charge transfer along the PBDT-TS1 polymer backbone.

The vertical energy gap ΔE_{DA} results in a negative sign (Fig. 4.37) for all $\theta(\mathbf{AB})$ and $\theta(\mathbf{BA})$ in the range $[-180^\circ, 180^\circ]$. In the **AB** sequence, the data reveals a plateau about $\theta = -90^\circ$ to 90° , whereas the values for the **BA** sequence gives rise to an M-shaped pattern. The values for $\Delta E_{DA}^h(\theta(\mathbf{AB}))$ are in the range between -0.94 eV and -1.05 eV, while $\Delta E_{DA}^h(\theta(\mathbf{BA}))$ gives values between -0.63 eV and -0.86 eV and the central maximum is -0.72 eV around the $\theta = 0^\circ$ configuration. The sign of ΔE_{DA}^h indicates enhanced intra-chain hole transport abilities of PBDT-TS1.

The vertical energy gaps $\Delta E_{DA}^e(\theta(\mathbf{AB}))$ and $\Delta E_{DA}^e(\theta(\mathbf{BA}))$ from CDFT/PBE calculations possess a positive sign and exhibit only small variations in the magnitude 0.15 eV (**AB**) and 0.13 eV (**BA**) as a function of the dihedral angle (Fig. 4.38). So, one obtains about 0.1 eV higher average values for $\theta(\mathbf{BA})$ with $\bar{\Delta E}_{DA}^e = 0.43$ eV than for $\theta(\mathbf{AB})$ with about $\bar{\Delta E}_{DA}^e = 0.33$ eV.

All in all, the intramolecular charge transfer integrals $|J_{DA}^{\text{int}}|$ and internal vertical energy gap $\Delta E_{DA}^{\text{int}}$ exhibit a high magnitude in PBDT-TS1. They are interpolated by spline fits as a function of the SCCS dihedral angles $\theta(\mathbf{AB})$ and $\theta(\mathbf{BA})$ for the intramolecular hole and electron transport along the polymer chain backbone and these values enter the Marcus, Jortner or Weiss-Dorsey rate expressions for intramolecular charge transfer.

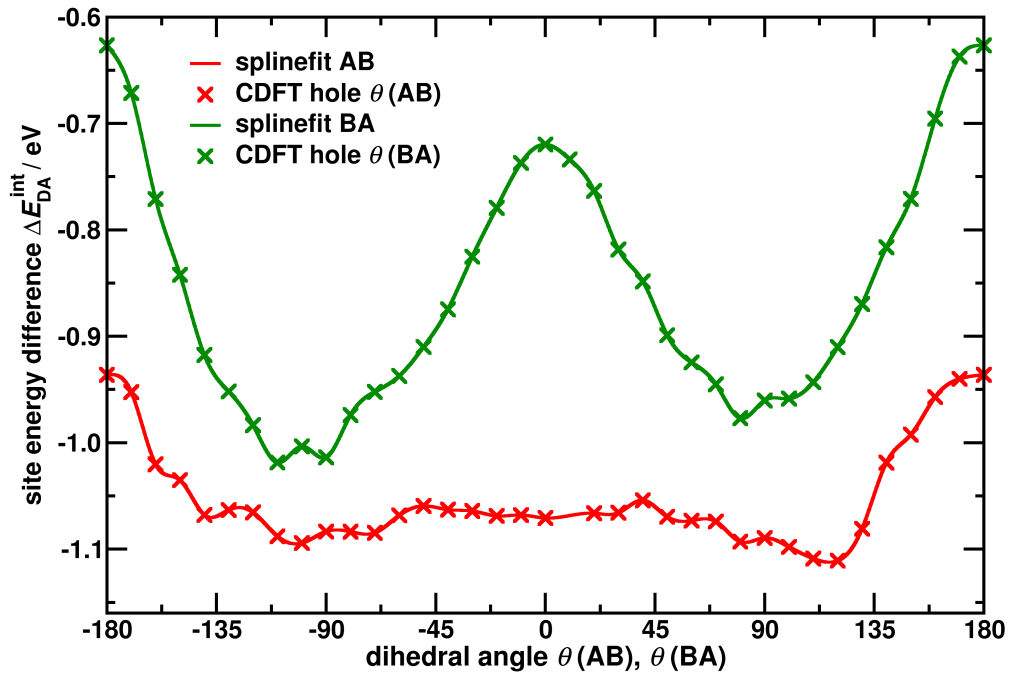


Figure 4.37: Internal vertical energy gap $\Delta E_{\text{DA}}^{\text{int}}(\theta(\text{AB}))$ and $\Delta E_{\text{DA}}^{\text{int}}(\theta(\text{BA}))$ for hole transport on CDFT/PBE level of theory as a function of the dihedral angles $\theta(\text{AB})$ and $\theta(\text{BA})$ between PBDT-TS1 subunits in **AB** and **BA** sequence order. Spline fits interpolate the data.

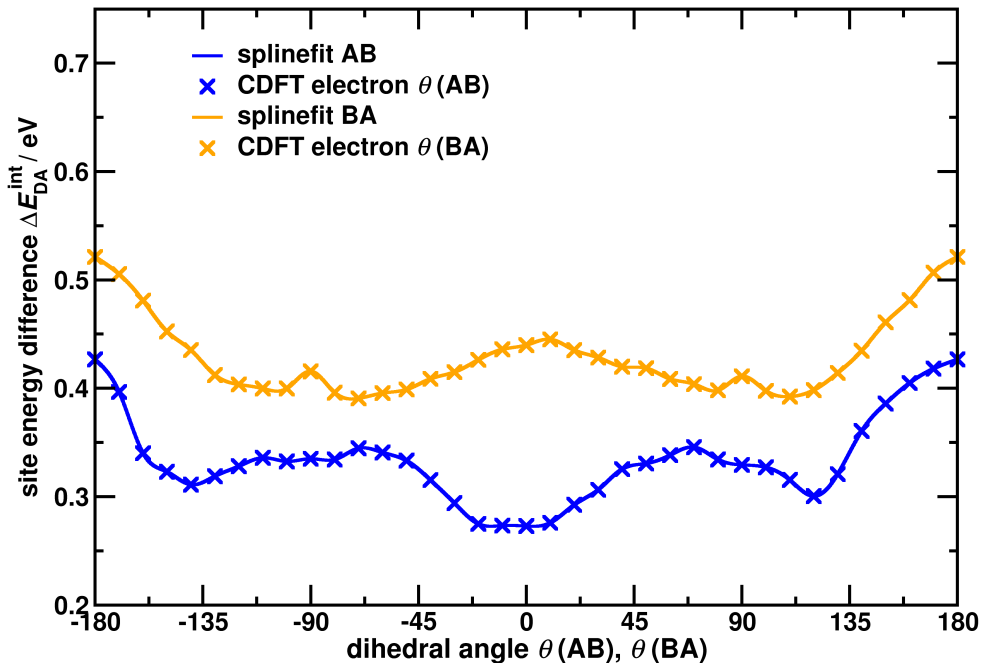


Figure 4.38: Internal vertical energy gap $\Delta E_{\text{DA}}^{\text{int}}(\theta(\text{AB}))$ and $\Delta E_{\text{DA}}^{\text{int}}(\theta(\text{BA}))$ for electron transport on CDFT/PBE level of theory as a function of the dihedral angles $\theta(\text{AB})$ and $\theta(\text{BA})$ between PBDT-TS1 subunits in **AB** and **BA** sequence order.

4.2.5 Internal Reorganization Energy and Site-energy Difference

In the following, we focus on charge transfer between a PPDI molecule and another PPDI or a PBDT-TS1 segment as a function of the polymer chain length l . Therefore, we optimised the structures of isolated molecules and polymer segments in the vacuum on DFT/B3LYP/6-31G* level of theory in order to describe hole and electron transfer in $\text{PPDI} \leftrightarrow \text{PBDT-TS1}$ and $\text{PPDI} \leftrightarrow \text{PPDI}$ transitions.

The Figure 4.39 displays the internal reorganization energies λ_h^{in} , λ_e^{in} and internal site-energy difference ΔE_h^{in} , ΔE_e^{in} . The internal reorganization energy is $\lambda_h^{\text{in}} = 0.081$ eV for hole transfer between two neighbouring PPDI molecules, whereas the reorganization energy for electron transfer $\lambda_e^{\text{in}} = 0.135$ eV is higher. The reduction of the aliphatic side chains to propyl groups is a suitable approximation for the determination of the internal reorganization energy, as one obtains only slightly higher values (4 meV) as $\lambda_h^{\text{in}} = 0.084$ eV and $\lambda_e^{\text{in}} = 0.139$ eV for $\text{PPDI} \rightarrow \text{PPDI}$ transitions in case of including the side chains.

In general, the reorganization energy for hole transfer for $\text{PPDI} \rightarrow \text{PBDT-TS1}$ yields higher values than the corresponding data for electron transfer. One obtains $\lambda_h^{\text{in}} = 0.175$ eV for hole transfer to a segment of type **A** and a maximum value $\lambda_h^{\text{in}} = 0.496$ eV to a segment of type **B**. An increase in the chain length reduces the value to a limit of $\lambda_h^{\text{in}} = 0.085$ eV for a chain with $n=8$ alternating **A** and **B** units ($\mathbf{A}_8\mathbf{B}_8$). Accordingly, the inverse direction $\text{PBDT-TS1} \rightarrow \text{PPDI}$ yields $\lambda_h^{\text{in}} = 0.186$ eV for segment **A** to PPDI, it exhibits a maximum at $\lambda_h^{\text{in}} = 0.360$ eV for segment **B**, and decays to a similar limit $\lambda_h^{\text{in}} = 0.088$ eV for $\mathbf{A}_8\mathbf{B}_8 \rightarrow \text{PPDI}$.

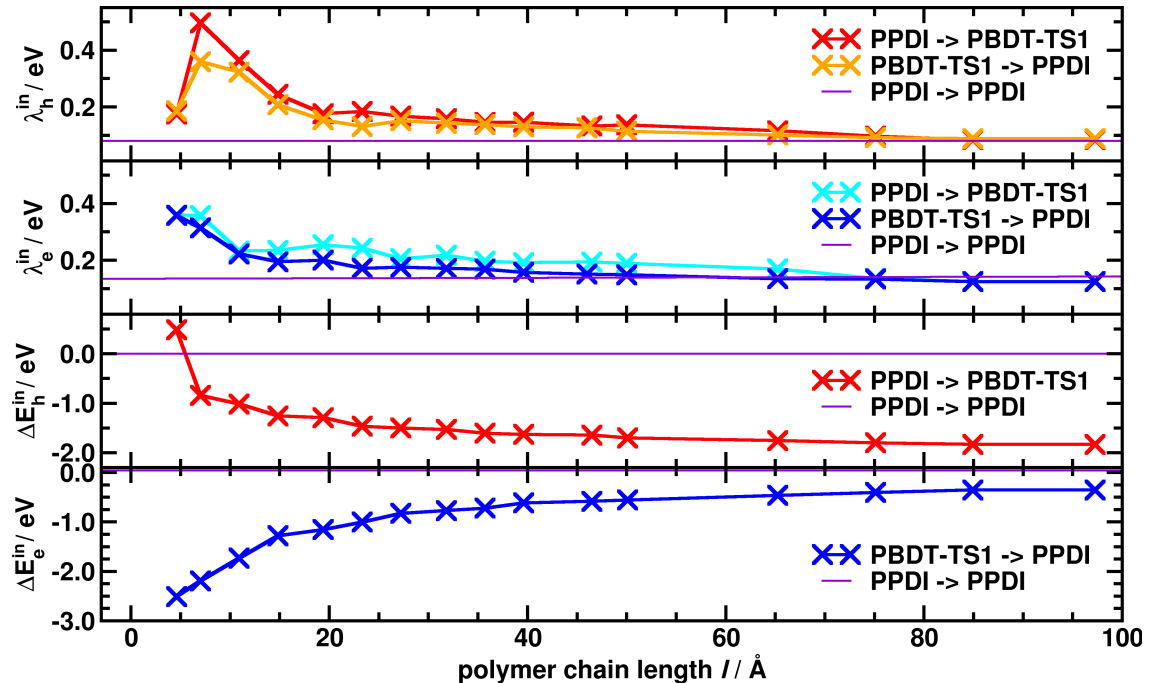


Figure 4.39: Internal reorganization energy $\lambda_{h/e}^{\text{in}}$ and internal site-energy difference $\Delta E_{h/e}^{\text{in}}$ for a hole (red, orange) and electron (cyan, blue) transfer in $\text{PPDI} \rightarrow \text{PBDT-TS1}$, $\text{PBDT-TS1} \rightarrow \text{PPDI}$ and $\text{PPDI} \rightarrow \text{PPDI}$ (violet) transitions at DFT/B3LYP/6-31G* level of theory on vacuum level. The data for the polymer PBDT-TS1 is displayed as a function of the chain length l including the sequences $\mathbf{A}_n\mathbf{B}_n$ with $n \in [1, 8]$ as well as $\mathbf{A}_n\mathbf{B}_{n-1}$ and $\mathbf{A}_{n-1}\mathbf{B}_n$ with $n \in [1, 4]$.

For PPDI \rightarrow PBDT-TS1 electron transfer, we obtain $\lambda_e^{\text{in}} = 0.360$ eV to unit **A** and $\lambda_e^{\text{in}} = 0.358$ eV to unit **B**. The electron internal reorganization energy decays to $\lambda_e^{\text{in}} = 0.125$ eV in the long-chain limit. The PBDT-TS1 \rightarrow PPDI transitions for the opposite direction yield $\lambda_e^{\text{in}} = 0.358$ eV for a transition from **A** to PPDI, $\lambda_e^{\text{in}} = 0.354$ eV for **B** to PPDI and the reorganization energy declines to a similar limit of $\lambda_e^{\text{in}} = 0.125$ eV for **A**₈**B**₈ \rightarrow PPDI. Accordingly, the dependence of $\lambda_{\text{h/e}}^{\text{in}}$ on the direction of charge transfer is small in PBDT-TS1 \leftrightarrow PPDI transitions.

The internal site-energy difference yields a value of $\Delta E_{\text{h}}^{\text{in}} = 0.484$ eV for hole transfer in PPDI \rightarrow **A** transitions, and decays for longer PBDT-TS1 chains from -0.843 eV to -1.832 eV. PBDT-TS1 \rightarrow PPDI transitions yield a negative sign for the internal site-energy difference ΔE_e^{in} and rise from -2.510 eV to -0.353 eV. This is in accordance with the preferential transfer direction PPDI \rightarrow PBDT-TS1 for holes and PBDT-TS1 \rightarrow PPDI for electrons in the blend.

The determined $\lambda_{\text{h/e}}^{\text{in}}$ and $\Delta E_{\text{h/e}}^{\text{in}}$ can vary by up to 0.2 eV (CAM-B3LYP) depending on the choice of functional and base set (A.3.1 Tab. A.4 and A.5). $\lambda_{\text{AB}}^{\text{in}}$ in combination with PBE0/6-31G* is similar to B3LYP/6-31G*. A higher basis set (6-31G**) results in an increase of $\lambda_{\text{AB}}^{\text{in}}$. We tabulate $\lambda_{\text{AB}}^{\text{in}}$ and $\Delta E_{\text{AB}}^{\text{in}}$ for more combinations of PBDT-TS1 \leftrightarrow PBDT-TS1 and PPDI \leftrightarrow PBDT-TS1 transitions (see A.3.1 Tab. A.6,A.7,A.8).

4.2.6 kMC Simulations in PBDT-TS1:PPDI

We simulate charge transport in an amorphous blend morphology with PBDT-TS1 and PPDI molecules (Fig. 4.40,i). The morphology does not show a clear donor-acceptor phase separation. The polymers do not exhibit a preferred direction in their alignment and neither crystalline nor semi-crystalline regions are present. Instead, we observe the formation of small PPDI clusters consisting of about four to ten PPDI molecules, which are embedded inside amorphous, randomly oriented PBDT-TS1 chains. The presence of these clusters is also visualised in the distribution of the hopping sites (Fig. 4.40,ii). Each PPDI molecule is regarded as a single hopping site, and we employ the dihedral angle $\theta_{\text{SCCS}}^{\text{cut}}=60^\circ$ as a cutoff criterion for the partitioning of the polymer into segments (see Figs. 2.4 and 2.5).

We take a look at experimental mobilities for PBDT-TS1 and PPDI. The hole mobility is reported to be about $\mu^{\text{h}} = 1 \times 10^{-2}$ cm²/Vs for PBDT-TS1 in space-charge-limited current (SCLC) experiments [390]. The pristine PPDI film yields an electron mobility up to $\mu^{\text{e}} = 4.1 \times 10^{-4}$ cm²/Vs. The PBDT-TS1:PPDI blend films exhibit an electron mobility of $\mu^{\text{e}} = 1.2 \times 10^{-3}$ cm²/Vs and a hole mobility of $\mu^{\text{h}} = 8.9 \times 10^{-3}$ cm²/Vs, which indicates a balanced device performance based on measurements in hole-only and electron-only diodes.

We perform kMC simulations in the PBDT-TS1:PPDI blend and compare mobilities obtained for different rate expressions for hole and electron transfer (Tab. 4.2). The simulations include intermolecular and intramolecular charge transport. The simulated mobilities are several orders of magnitude below the experimental results. Even, the experimental trend of enhanced μ^{h} compared to μ^{e} in the blend is not reflected in the data based on kMC simulations. Only Weiss-Dorsey rates for electron transport reach the magnitude of experimental results. The Marcus rates for electron transport do not reflect the correct charge transfer direction at the donor-acceptor interface in PBDT-TS1:PPDI. It is a similar deficiency as found in P3HT:DIPBI (see Sec. 4.1.3.8). Hence, the kMC simulations with Marcus rates sample mainly trajectories on PBDT-TS1, where $\mu_{\text{tot}}^{\text{h}}$ and $\mu_{\text{tot}}^{\text{e}}$ are similar. A direct comparability of experimental to kMC mobilities is not given primarily due to the absence of any crystalline domains and missing side chains in the MM morphology.

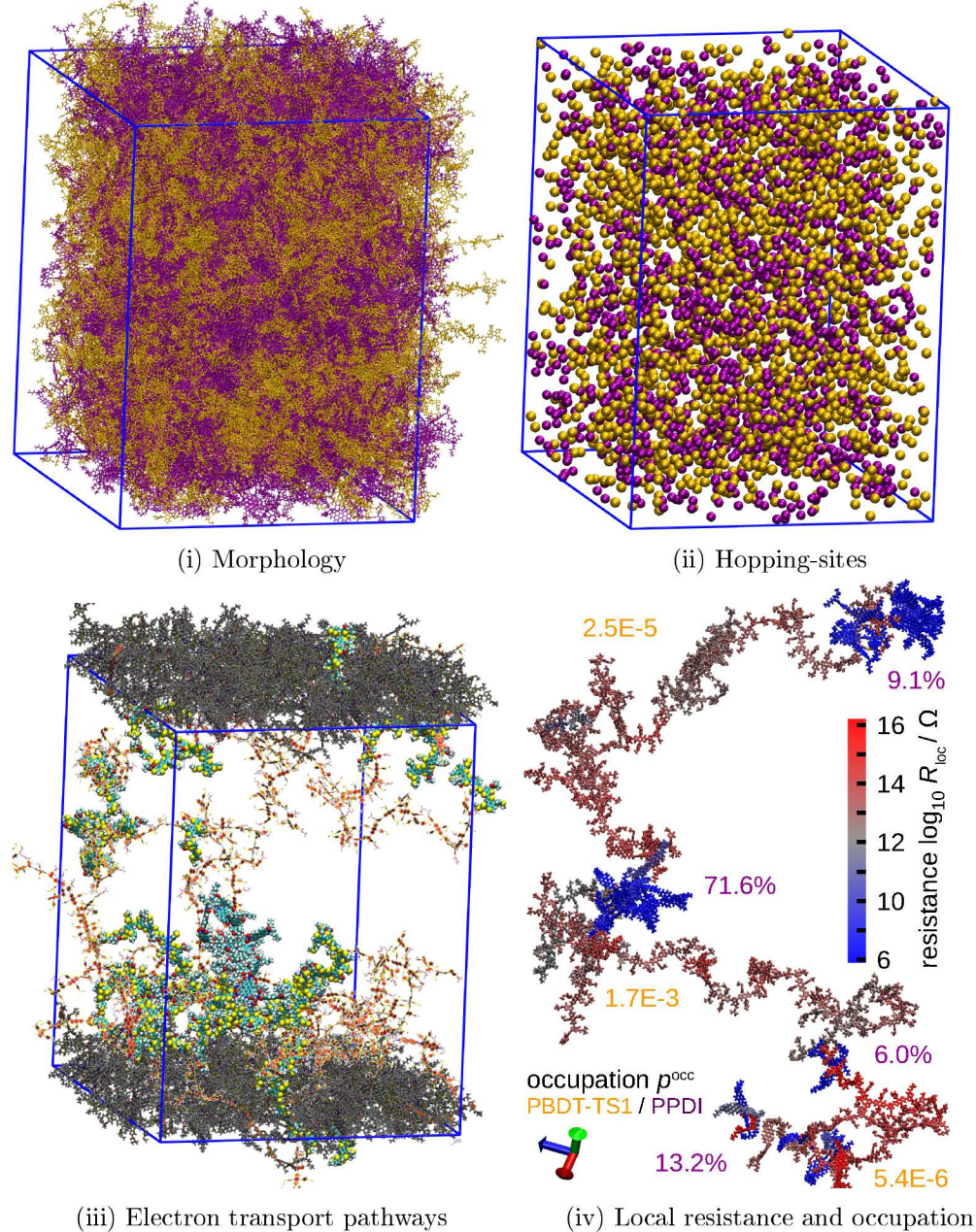


Figure 4.40: (i) Amorphous blend morphology with donor polymer PBDT-TS1 (yellow) and acceptor PPDI (violet). (ii) Distribution of hopping sites using a cutoff angle $\theta_{\text{SCCS}}^{\text{cut}} = 60^\circ$ for the partitioning of PBDT-TS1. (iii) Electron transport pathways with small electronic resistance based on Weiss-Dorsey transfer rates using the Dijkstra algorithm. We determine pathways connecting every molecule in the start zone (black, below) with the end zone (black, above). The molecules on pathways are depicted in paper chain representation (orange), and the pathway with the lowest total resistance $|R^{\text{tot}}|$ is depicted in VdW representation. Note that the continuous pathways contain linked images using periodic boundary conditions. (iv) Single-electron transport pathway with local resistance $\log_{10} R_{\text{loc}}$ (red, blue colour-coded) and the occupation p_e^{occ} of PBDT-TS1 sections (orange) and PPDI clusters (violet).

Table 4.2: Hole mobility $\mu_{\text{tot}}^{\text{h}}$ and electron mobility $\mu_{\text{tot}}^{\text{e}}$ in PBDT-TS1:PPDI blend.

	Marcus	Jortner	Weiss-Dorsey
$\mu_{\text{tot}}^{\text{h}}$ [cm ² /Vs]	(1.45 ± 0.92)E-8	(4.34 ± 3.61)E-10	(9.97 ± 5.67)E-7
$\mu_{\text{tot}}^{\text{e}}$ [cm ² /Vs]	(1.95 ± 1.53)E-8	(2.41 ± 1.70)E-7	(6.95 ± 2.42)E-4

In the following, we analyse the kMC simulations using Weiss-Dorsey rates in more detail. We notice that the majority of electron transitions 99.96% in kMC simulations occurs between hopping pairs of the electron acceptor molecule PPDI. So, about 0.04% of all electron transitions are in the donor domain. They can be sub-divided into 96.4% intra-chain transitions and 3.6% inter-chain transitions between two PBDT-TS1. The share of 1.7×10^{-8} PBDT-TS1→PPDI transitions exceeds those in the opposite direction 1.5×10^{-8} PPDI→PBDT-TS1. These rare events reflect the expected predominant electron transfer direction at the donor/acceptor interface correctly.

As the morphology does not exhibit clear donor-acceptor phase separation, we do not find continuous electron pathways crossing the box that only consists of PPDI molecules. We find that a high number of PPDI→PPDI transitions occur inside the small PPDI clusters. Conductive PBDT-TS1 chains link these clusters. If we take a look at the low resistance pathways for electron transport crossing the simulation box (Fig. 4.40,iii), we note a high number of PBDT-TS1 chains contribute to the pathways. In this morphology, the spatial advance in field direction of the electrons occurs predominantly on PBDT-TS1 through combinations of inter and intra-chain transitions, although the number of PPDI→PPDI transitions is significantly higher in the isolated clusters.

The electron transport within the PPDI clusters results in a remarkable lower resistance than the transport along the PBDT-TS1 chains. The average resistance along the pathways is $\log_{10} \bar{R}_{\text{loc}}^{\text{e}} = (7.92 \pm 3.02) \Omega$ on PPDI, which is lower than the corresponding value for PBDT-TS1 segments $(12.22 \pm 1.07) \Omega$. This difference is visualised in the colour-coded representation of a selected low resistance pathway (Fig. 4.40,iv). It contains 44 PPDI molecules that form four clusters, which are linked by winding 31 PBDT-TS1 molecules that partitioned into 66 segments.

The electron remains predominantly on PPDI clusters, where we find high occupation numbers, e.g. $p_{\text{e}}^{\text{occ}} = 13.2\%$, 71.5% and 9.1%. Even a small aggregate of three PPDI yields a contributes of 6% to the total occupation. In contrast, the occupations on PBDT-TS1 sections sum to local occupation numbers, which are several orders of magnitude lower values, e.g. 5.4×10^{-6} , 1.7×10^{-3} and 2.5×10^{-5} . As a consequence, the electron is mainly trapped on PPDI clusters, until it can escape to a PBDT-TS1 segment and travels in a random walk till reaching the boundary of a next PPDI cluster, where the electron is temporarily captured again. It corroborates our finding from visual inspection of single-electron kMC trajectories. In total, we observe the processes of a trap release mechanism for electron transport in amorphous PBDT-TS1:PPDI, where local impurities of the acceptor molecules inside the donor domain act as local traps.

The electron occupation number $p_{\text{e}}^{\text{occ}}$ for Weiss-Dorsey rates in the PBDT-TS1:PPDI blend yield the high average values for PPDI (Fig. 4.41,i, violet) and a segment **A**. The **B** segment exhibits a lower $p_{\text{e}}^{\text{occ}}$. We find an overall trend for lower occupation numbers with increasing chain length l , which is superimposed by a sawtooth pattern with a tip down at every third segment. This occurs for segments with $\mathbf{A}_{n-1}\mathbf{B}_n$ shape with $n \in [1, 8]$, where the number of units **B** exceeds the number of units **A**.

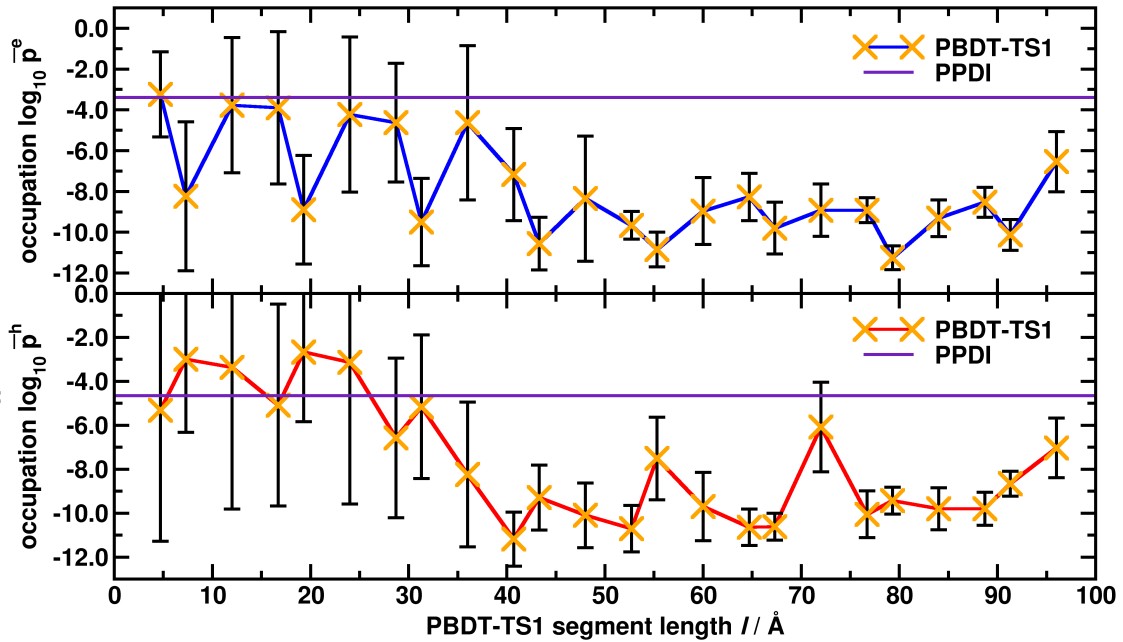


Figure 4.41: Occupation numbers for electron transport p_e^{occ} (above) and hole transport p_h^{occ} (below) in the PBDT-TS1:PPDI blend as a function of the PBDT-TS1 segment length l and for PPDI (violet) for comparison based on kMC simulations using Weiss-Dorsey rates.

The low resistance pathways for hole transport are mainly made up of PBDT-TS1 segments (95%) (Fig. 4.42,i). The minimum resistance pathway with $\log_{10} R_h^{\min} = 15.4 \Omega$ does not include any PPDI molecules. It contains 64% intermolecular transitions between PBDT-TS1 chains and 36% intramolecular transitions. There are several competing pathways with a small total resistance $\log_{10} R_h^{\text{tot}} \approx 15.7 \Omega$ (Fig. 4.42,ii).

The average resistance for hole transport along the pathways is $\log_{10} \bar{R}_{\text{loc}}^h = (13.61 \pm 1.16) \Omega$ on PBDT-TS1 segments, which is similar to the value $(13.46 \pm 1.97) \Omega$ obtained on PPDI. The latter is significantly higher than the corresponding value for electron transport. This is another indicator for the enhanced electron transport in PPDI, whereas the \bar{R}_{loc}^e is only slightly lower in PBDT-TS1 than \bar{R}_{loc}^h . If we analyse all hole pathways, we find that normally the transition with the highest local resistance determines about 98% of the total value for an entire pathway. For instance, the minimum resistance pathway exhibits an unpartitioned PBDT-TS1 chain with small torsion angles that possesses high resistance and an elevated occupation time (Fig. 4.42,iv). So, the $\mathbf{A}_8\mathbf{B}_8$ segment acts as a local hole trap. The charge transport across the donor-acceptor interface yields on average an elevated local resistance of $\log_{10} \bar{R}_{\text{loc}}^h = (16.9 \pm 3.34) \Omega$ and hence the mobility is reduced when compared to pure PBDT-TS1 pathways. Therefore, the domain boundary hinders charge transport. The visualisation of the charge transport pathways in combination with local resistance and the occupation time (Fig. 4.42) helps to understand electron and hole transport. However, it remains a challenging task to deduce a one to one correspondence between structural characteristics in the amorphous phase and beneficial charge transport properties.

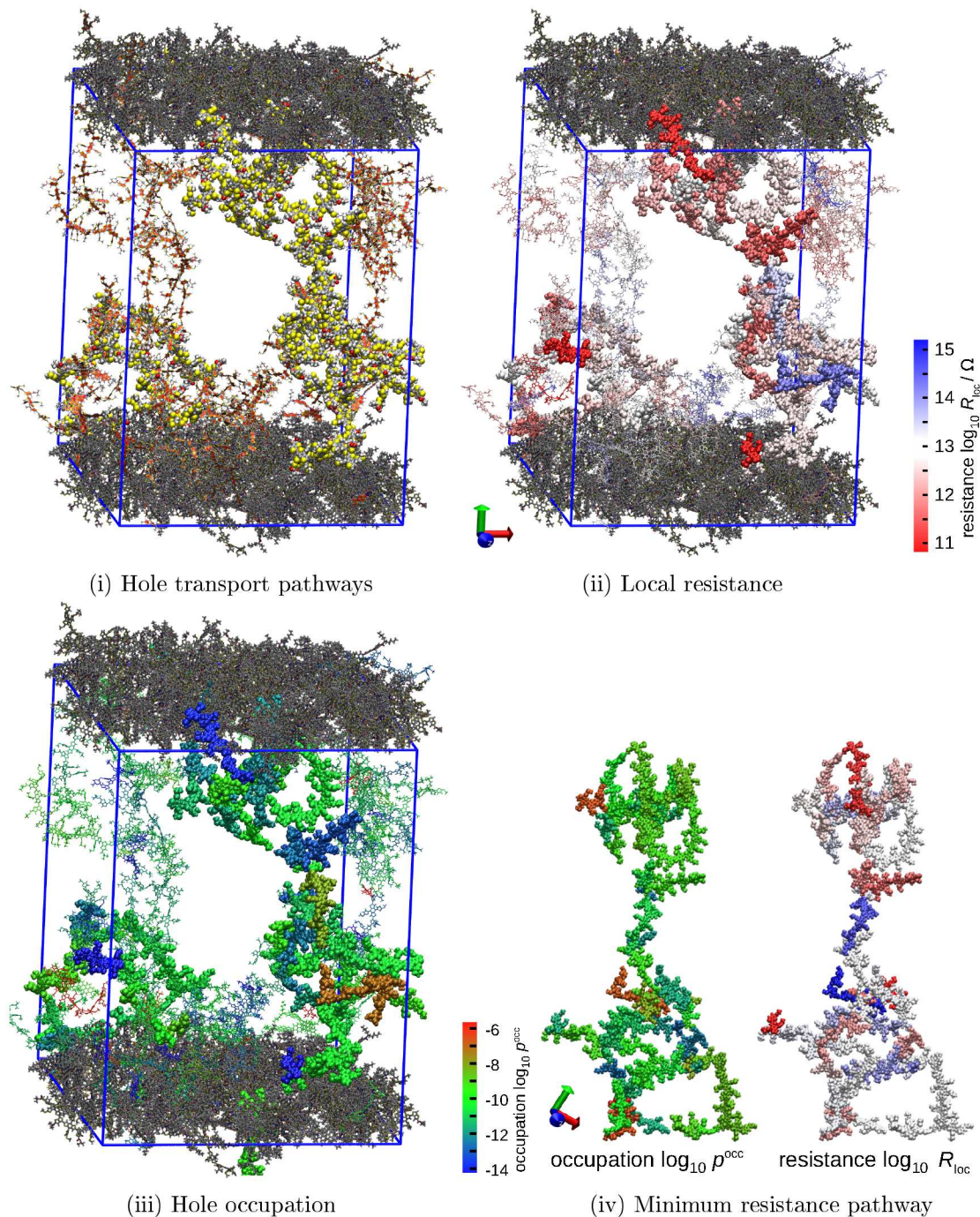


Figure 4.42: (i) Hole transport pathways with small electronic resistance based on Weiss-Dorsey transfer rates using the Dijkstra algorithm. We determine pathways connecting every molecule in the start zone (black, below) with the end zone (black, above). The molecules, which belong to the pathways are depicted in the paper chain representation (orange) and the one with the lowest total resistance $|R^{tot}|$ is depicted in VdW representation. (ii) Hole transport pathways with local resistance $\log_{10} R_{loc}^h$ and (iii) the occupation numbers $\log_{10} p_h^{occ}$. (iv) Minimum resistance pathway.